Vision-based Indoor Navigation of a Semi-autonomous and Interactive Unmanned Aerial System

Undergraduate Thesis

Presented in Partial Fulfillment of the Requirements for the Bachelor of Science with Research Distinction in the Undergraduate School of The Ohio State University

By

Hongyun Elliot Lee

Undergraduate Program in Aeronautical and Astronautical Engineering

The Ohio State University

Department of Mechanical and Aerospace Engineering

April 2017

Thesis Committee:

Dr. Matthew McCrink, Adviser

Dr. Clifford A. Whitfield

Copyright by

Hongyun Lee

2017

Abstract

This paper considers the development and implementation of a vision-based onboard flight management computer (FMC) and inertial navigation system (INS) that can estimate and control the attitude and relative position of the vehicle while interacting with an operator in an indoor environment. In this project, a hexacopter is developed which uses an onboard inertial measurement unit (IMU), a small-sized computer, and a Microsoft Kinect sensor. Since directional maneuver of the hexacopter can be achieved by changing the angular position of the vehicle, the project consists of inertial and vision sensor fusion.

To accomplish stable control of the multicopter's orientation, a complementary filter is implemented on the IMU. Since the raw sensors do not provide an accurate angular position of the vehicle per se, the complementary filter is used to fuse the raw sensor data to provide low-noise and low-drift estimation of Euler angles. Autonomous indoor flight requires position sensors other than GPS whose accuracy is approximately 2 to 3 meters. GPS signals are typically unavailable in an indoor environment. In this project, a computer vision algorithm is used to provide position estimation. The vision algorithm uses an onboard Microsoft Kinect and a computer to execute EmguCV and Kinect SDK libraries. Since Kinect can provide color and depth data, it allows to detect an object and to provide its real-time local coordinates which can be used for an autonomous indoor flight. The coordinates are used to correct the position of the vehicle. Also, to input commands such as takeoff, landing, proceed, retreat during the flight, an

artificial neural network is used to classify human gestures so that the gesture can be used as the commands.

The system is expected to maintain vehicle position within 1 meter for the better accuracy when compared to low-cost GPS receivers, and to control corresponding angular orientation for the position control. Also, the system is expected to interact with an operator within a reasonable interaction while it can maintain the given flight control tasks.

Dedication

I dedicate this paper to my family.

Acknowledgements

My work would have been impossible without my advisers. I would like to express my gratitude to them. Dr. Whitfield offered me a lab space to work on and supported my idea and advised the directions for the project from the very beginning to the end. I also learned a lot form Dr. McCrink about knowledge and concepts. He always supported me when I was having difficult time to understand them. My struggles became a part of this work and that was possible because of my advisers' guidance. Again, I sincerely appreciate their efforts.

I also appreciate my family who supported my education abroad in the U.S. It must be difficult decision to my parents, especially, due to the fiscal aspect. Finally, to all my friends who provided their supports and feedbacks, thank you.

Table of Contents

List of Tables

List of Figures

Chapter 1. Introduction

1.1 Overview

Unmanned aerial systems (UAS) and unmanned aerial vehicles (UAV) are playing important roles in this century due to its versatile functionalities that can conduct various flight-related tasks. One of UASs, Remote-Controlled (RC) multicopters has become frequently utilized from the public to the government level. Many fields like film industries and logistics companies use the multicopters. For instance, Amazon Prime Air recently submitted a petition to U.S Federal Aviation Administration for their R&D using UAS as package delivery systems [1].

For government-military related missions, the roles for the UAS pilots are significant to operate the UAS missions. However, operating the UAS with a group of pilots have difficulties due to human factors such as fatigue, miscommunication, attention, and workload [2]. To reduce the load of pilots and augment the performance of the UAS operations, based on a study by Drury, a detailed framework system that can manage the amount of mission flight information and transfer it to the operators was proposed [3]. For example, by authorizing an UAS to sufficiently handle necessary tasks such as autonomous obstacle avoidance, the information load for human pilots can be reduced. In a study by Call et al., it has been shown that an UAS can avoid obstacles using vision sensors [4].

On the other hand, there are other non-military usages of the drone as well [5]. The civilian usages such as logistics, sports, and entertainment are rapidly growing based on the

development of computing technology. Early human-computer interaction (HCI) was achieved in 1980 to recognize human gestures and voices [6]. Nowadays, HCI technologies are widely used in the daily lives as mobile platforms or as peripheral devices [7-10]. Using such devices, many human-robot interaction (HRI) applications for both remote and embedded systems have been introduced [11-13]. Also, multirotor-specific applications have been presented using visual devices [14-17]. Not surprisingly, the visual devices can provide the relative position of the drone so that it can be used in a GPS-denied situation while a particular camera such as Kinect is exploited to enable real-time HRI during the flight.

1.2 Objective

The purpose of this work is to develop an onboard Kinect-based hexacopter and its inertial navigation system (INS) that can track and follow an object with specific color or a body part while it can recognize human gestures. The primary purposes of the project are:
(1) Development of an inertial measurement unit (IMU) for the robust attitude control and the visual frame rotation. (2) Implementation of a color and a body part tracking algorithms. (3) Classification of the operator's body gestures. (4) Integration of an INS for the semi-autonomous flight. (5) Development of a small-scale ground control station (GCS). In this work, Microsoft Kinect is used while the Tarot FY 680 is used as the vehicle frame [9, 18].

In the previous works, an A.R. drone is used since it provides the framework to the vehicle via wireless local or global network connections [14-17]. In particular, Ambühl successfully implemented an UAV that can change its position by tracking an operator hand's 3D coordinate [14]. Also, Sanna et al successfully implemented to interface human gestures using flexible action and articulated skeleton toolkit (FAAST) [15, 20]. In the both works, the camera device is located on the ground. Thiang et al used an onboard camera to track a specific color using 2D coordinate

tracking [17]. Indeed, this paper shows the navigation of the hexacopter using the relative local 3D coordinate of the user or an object with a specific color. Using a ground Kinect can be useful for navigation over a path with unknown distance [15]. In this work, mounting Kinect is attempted to reduce equipment such as cameras and the internet set up in the indoor environment. The work by Sanna et al provides robust navigation of the drone when the target does not present in the frame of the camera. Also, FAAST offers robust gesture recognition output whereas, in this work, artificial neural network (ANN) is trained and implemented to classify user-defined natural gestures.

In this context, this project is composed of three sections. The developments of an onboard INS development, an onboard camera and its image processing and flight management computer, and a ground control station. In chapter 2, the hardware parts and circuit development processes are discussed. In chapter 3, a detailed IMU algorithm is presented. Chapter 4 discusses the object detection, real-time gesture classifier, and flight management algorithms. In chapter 5, INS integration, controller, and its performance are shown. Chapter 5 shows the ground control software. Finally, chapter 7 discusses the results and future works.

Chapter 2. System Overview

2.1 Hardware

In this chapter, hardware parts used for the hexacopter are introduced. For the airframe, Tarot FY 680 is chosen along with DJI E800 propulsion system [21]. It is powered by a 6-cell lithium-polymer battery. For flight manage computer, Intel NUC is mounted [22]. Also, four Parallax Propeller micro controller unit (MCU) are used as shown in figure 2.1 [23]. The onboard system has onboard sensors, MPU9250, PING ultrasonic distance sensor, HMC5883L, and Microsoft Kinect [9, 24, 25, 29]. The hardware parts all together build an INS and a flight management computer (FMC).

For the ground station, a Windows 10 based computer with .NET framework and a joystick driver, Slim DX SDK and a joystick controller are exploited [26]. Also, for the communication between the onboard and the ground-based computers, a pair of XBee radio module is connected [27]. The table 2.1 lists the weights of the vehicle parts.

Table 2.1 Weights of the vehicle parts

Hexarotor System	Weight (kg_f)	Number	Total (kg_f)
Frame	1.32	1	1.32
ESC	0.043	6	0.258
Motor	0.106	6	0.636
Propeller	0.019	6	0.114
6s lipo	0.6555	1	0.6555
Cameras & mount	0.345	1	0.345
Electronic devices and miscellaneous	0.2	1	0.2
Total			3.5285

2.1.1. Vehicle Frame and Power System

Tarot FY680 is a hexacopter frame that has 695 mm diameter and 180 mm height. Hexarotor frame is desired to support the total weight of the body whose maximum weight is approximately 6 kg. DJI E800 propulsion package is composed of 6 sets of 1345 propeller, a 3510/350KV brushless direct current (BLDC) motor, and a 6S 20A electric speed controller (ESC). The 1345 propeller has 13 inches or 33 cm diameter and the pitch angle that can travel 4.5 inches or 11.43 cm per single revolution. The BLDC motor has a stator size of 35 mm × 10 mm and capability of 350 rpm per volt. Unlike conventional brushed DC motors, the BLDC motors do not use the brush but use a polarity-altering stator and permanent magnets. The BLDC motor is preferred because it is efficient and has robust output compared to brushed DC motors. To operate the BLDC motor, the ESC is used which expects a certain range of pulse width modulation (PWM). The ESC has input signal frequency spans from 30 Hz to 450 Hz. For the consistent control, synchronized ESC-motor performance is desired. DJI E800 propulsion system is pre-tuned by the manufacturer so that the same PWM input is guaranteed to output the same RPM for the given input PWM.

The operation range of a power system is shown in figure 2.2 c. The range of the motor thrust output between 0.2 kg_f to 1.2 kg_f is almost linear. As the input increase, the thrust decreases. Therefore, the most of the drone thrust variation in this project is confined to the linear range, 1400 ~ 1800 PWM. The maximum force of a motor within the linear range is 1.2kgf. The total weight of the vehicle is approximately 3.5 kg_f. With all six motors together, the maximum lift, $1.2 \times 6 = 7.2$ kg_f, which is still larger than the total weight of the vehicle, 3.5kg_f.

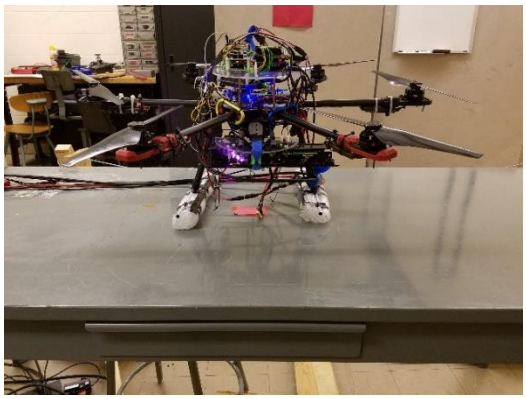

(a) Front view

(b) Side view

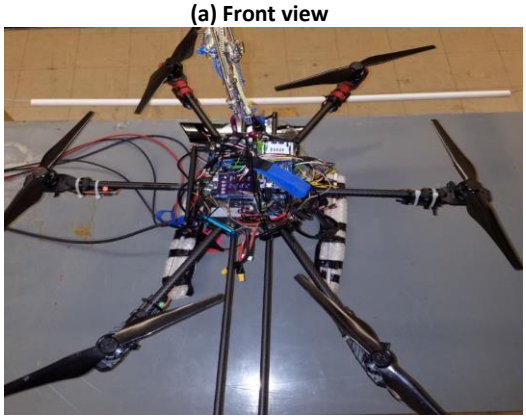

(c) Top view

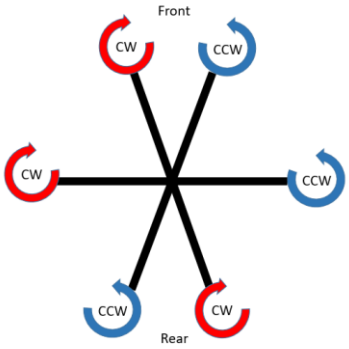

(d) Propeller rotation direction (top view)

Figure 2.1 Three views of the hexacopter

(a) A set of DJI E800: a propeller, BLDC motor, and ESC

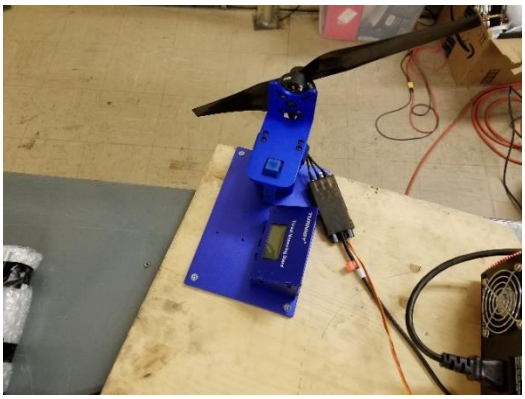

(b) Thrust measurement device

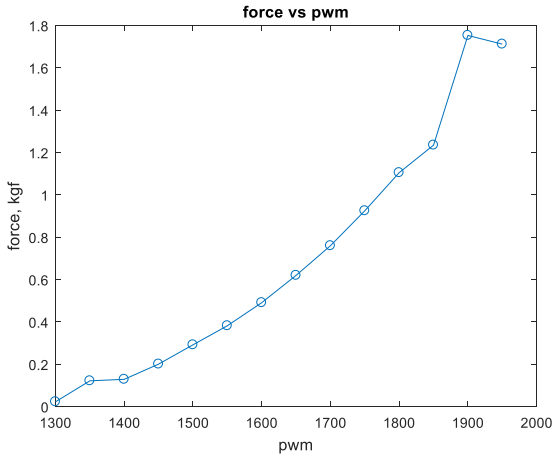

(c) Thrust of a power system at 22 v

Figure 2.2 Power system and its character

2.1.2 Sensors

To implement the INS, inertial and vision sensors are needed. Inertial sensors used in this work are a gyroscope, an accelerometer, and a magnetometer. The mounted vision sensors are a red green blue (RGB) camera and Kinect (RGB camera and a set of infrared light transmitter and the receiver). Also, to operate taking-off and landing with the RGB camera pointing ground an ultrasonic distance sensor is used. (See figure 2.4) In this work, the distance

sensor and Kinect's RGB camera are used to track color. The ground RGB camera is for the future purpose. The detail is discussed in Chapter 7.

For this project, two MPU 9250 boards are chosen for the inertial sensors since each board has the gyroscope, the accelerometer, and the magnetometer. Two MPU 9250 boards are used to maximize the sampling rate of the gyroscope and accelerometer so that the output rate of the attitude estimation can be up to 175Hz at maximum. Since the gyroscope and accelerometer on MPU 9250 share the same I2C line, the reading rate of the both sensors can decrease overall rate of the sensor reading [30]. Also, not to interfere the I2C lines of the both MPU9250 boards, an external magnetometer, HMC5883L is used [29]. To mount these sensors, printed circuit board (PCB) is designed using Eagle as shown in figure 2.3 [31]. The update rates of Kinect and the RGB camera are both 30 frames per second (FPS). The frames from Kinect are used for detecting a color of an object or body parts of an operator to estimate relative local coordinate of the target while the frames from the RGB camera are used for tracking the object with a specific color. Also, to estimate the distance to the floor of the indoor environment, a distance sensor, PING ultrasonic sensor is chosen, whose detection range is 0.3 meters to 3 meters at 40 kHz.

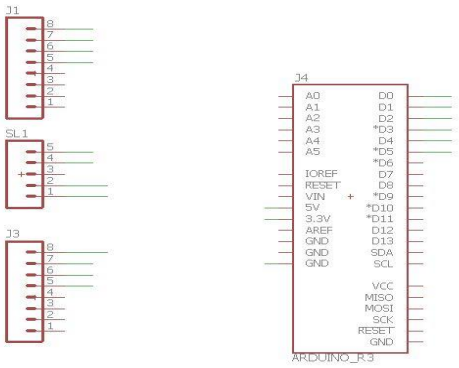

(a) Schematic of the sensor circuit

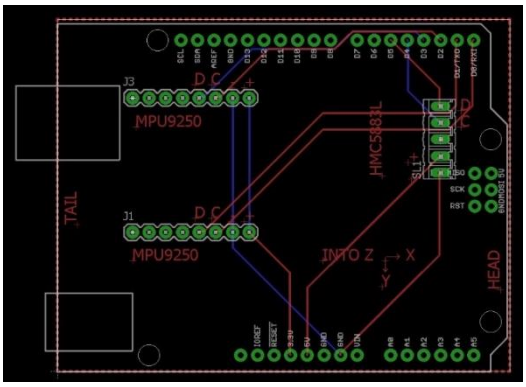

(b) Layout of the sensor circuit

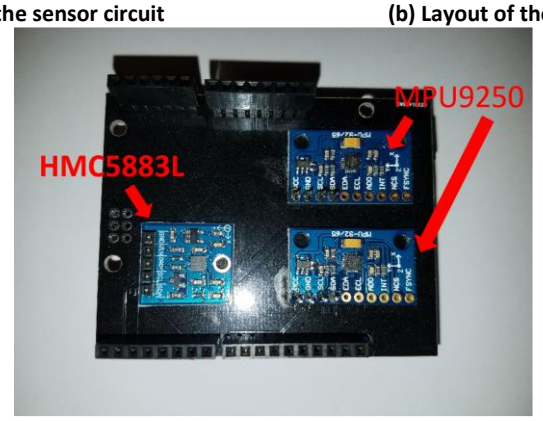

(c) The printed sensor circuit after soldering

Figure 2.3 PCB of IMU shield for Propeller ASC

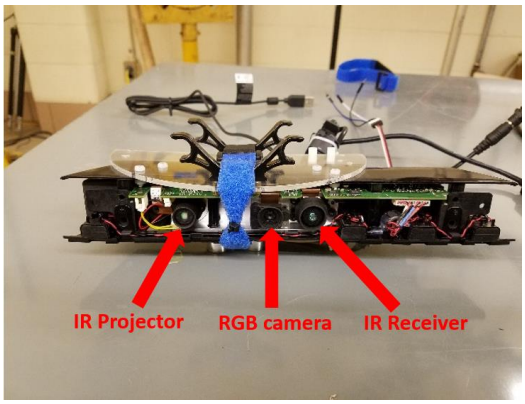

(a) Front view of the Kinect mount

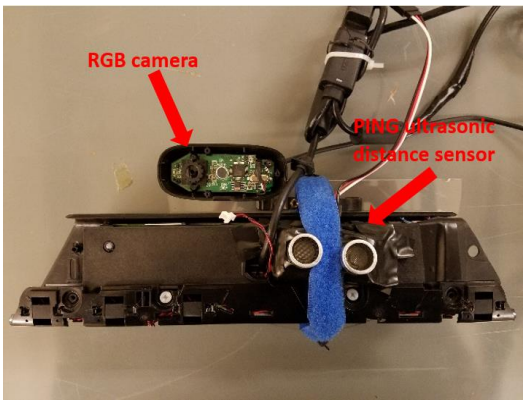

(b) Bottom view of the Kinect mount

Figure 2.4 Kinect and supplementary devices

2.1.3 Onboard Computers

The onboard computer is composed of two types: a computer with an operating system is used as the FMC, and the four MCUs are used to develop the INS as shown in figure 2.5. The

FMC is used to exploit vision sensor and managing basic operations such as take-off and landing. Also, the MCUs are used to operate as an inertial measurement unit (IMU), a controller, and a communication device. Intel NUC is used as FMC. The computer is operated by Windows 10. The maximum stock frequency of the CPU (Core i7-5557U) is at 3.1 GHz or 3.4 GHz at maximum.

For the microcontrollers, four Parallax Propeller boards and an Arduino boards are used. A Parallax MCU has eight cogs that can operate eight different tasks simultaneously without threading architecture on the processor. The stock frequency of the system clock is at 80 MHz, and it is overclocked to 100MHz to maximize the performance. The four onboard MCUs are used for sensor fusion, control, and communication with the ground control station and the FMC. The detailed is described in Chapter 5. An Arduino board is also incorporated to monitor battery status. Since monitoring battery level does not require high sampling rate, a 16MHz Arduino Micro board is chosen. The detailed battery voltage level monitoring circuit is discussed in chapter 2.1.7.

2.1.4 Battery

For flight system, a 6-cell 22V 12000 mAh lithium polymer (Lipo) battery and 23 mAh portable battery with 12 V DC output are used. Since the 6 ESC have $20\ \mathrm{A} \times 6 = 120\ \mathrm{A}$ at burst, the battery should be able to support such discharge rate. The 6s Lipo has 30C discharge rate, which can be converted to $30 \times 12 = 360\ \mathrm{A}$. Therefore, the battery can support 120 A of discharge.

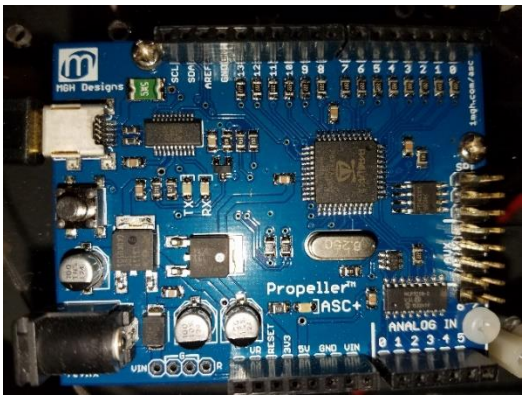

(a) Parallax Propeller ACS+ board

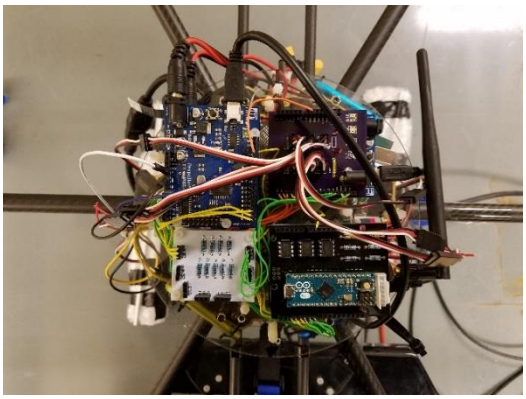

(b) Top view of the INS

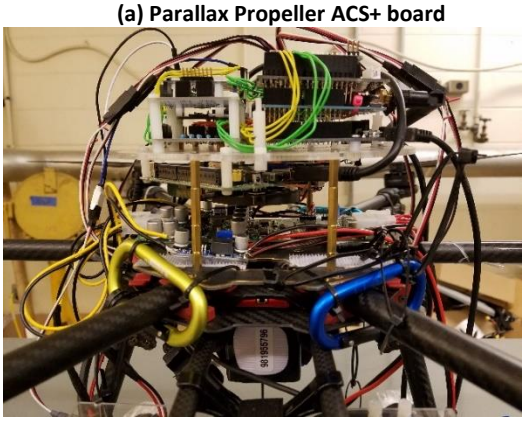

(c) Side view of the INS

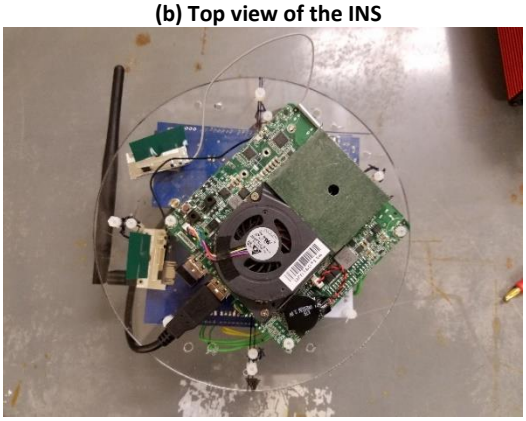

(d) Bottom view of the INS showing Intel NUC

Figure 2.5 The INS and FMC of the hexacopter

2.1.5 XBee

XBee is a radio communication module as shown in figure 2.6. The advantage of Xbee is that it interfaces radio communication for universal asynchronous receiver/transmitter (UART). The detailed discussion regarding communication via UART is addressed in Chapter 6.

Figure 2.6 Xbee module, antenna, and USB converter

2.1.6 DC to DC Buck Converter

As the vehicle consumes the power from the battery, the voltage level decreases. The general operation range of the 6s Lipo battery is 19v to 25v.To protect electronic devices such as Intel NUC and Kinect from varying voltage level, a DC to DC buck converter from Minibox is attached as shown in 2.7. The converter's input voltage range is from 6v to 36v while the output is constant 12v with 10A max. Similarly, two 12v to 5v buck step down buck converters are used to power the MCUs [32].

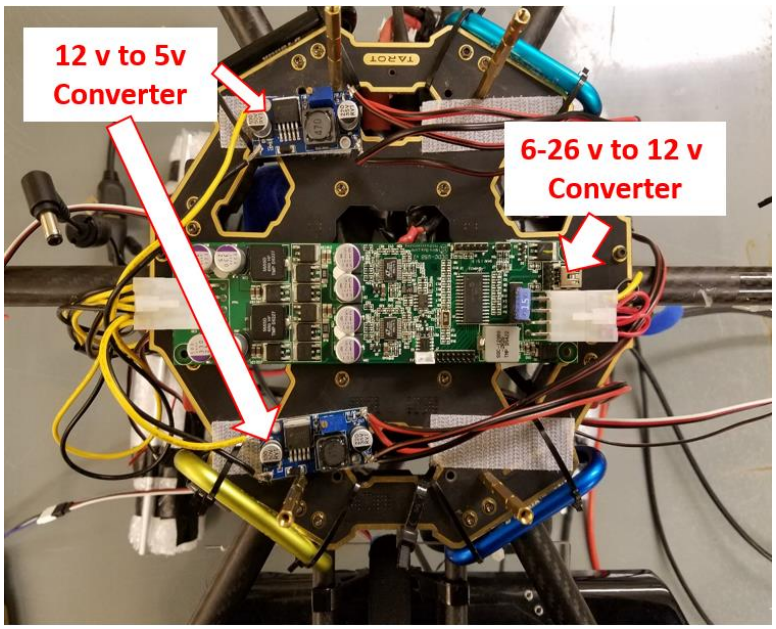

Figure 2.7 DC to DC converters

2.1.7 Voltage Divider-Follower Circuit

The shortage of the battery capacity during the flight can cause a severe damage for the system. To obviate any damage on electronic devices or structural frame due to the crash, the battery level needs to be monitored during the operation so that the flight plan can be changed to prepare for the landing.

The six cell Lipo battery is composed of six Lipo battery cells whose voltage range needs to be kept from 3.4 V to 4.3 V; otherwise, the battery can be damaged and needs to be disposed. Since the cells are connected in a series, the sixth cell's voltage level can go up to 25.8 V. For the microcontroller (Arduino micro) to be able to detect, the voltages of the cells need to be reduced to 5v max. Also, to protect the input voltage level from the internal circuit of Arduino, which affects the input voltage level the input circuit needs to be independent. Therefore, voltage divider and voltage follower circuits with resistors and op-amps are developed as shown in figure 2.8 [33].

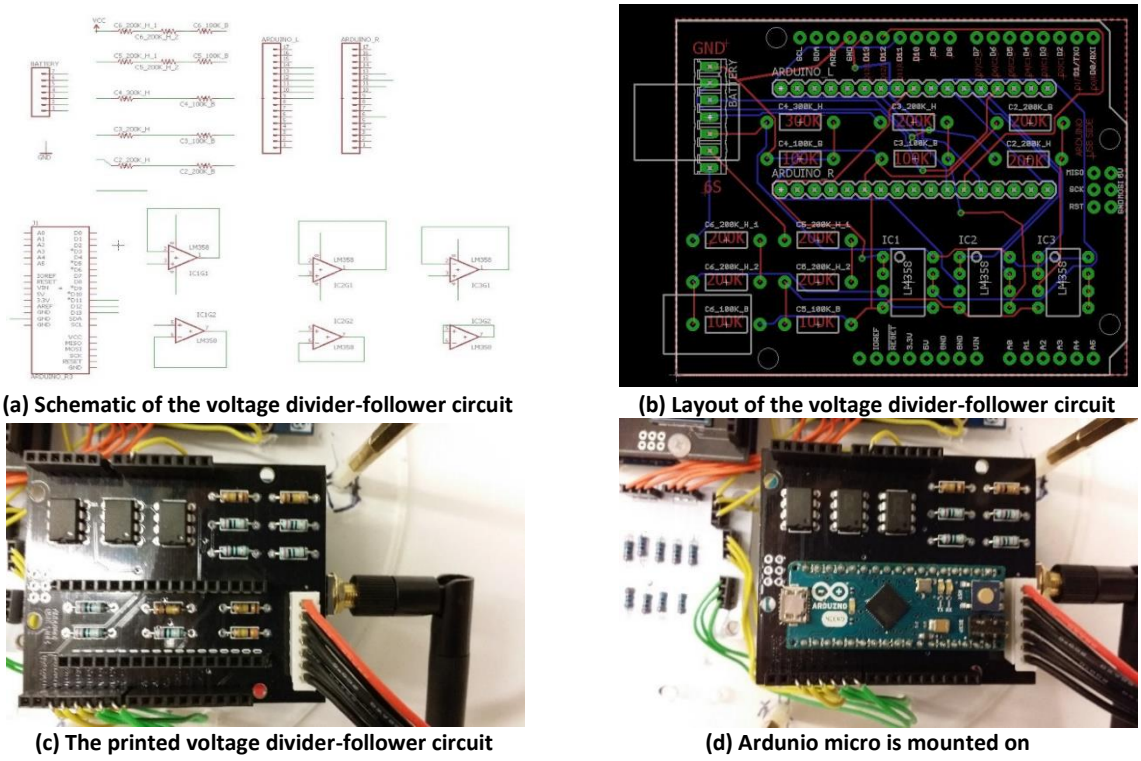

(a) Schematic of the voltage divider-follower circuit

(b) Layout of the voltage divider-follower circuit

(c) The printed voltage divider-follower circuit

(d) Ardunio micro is mounted on

Figure 2.8 Voltage divider-follower circuit

2.1.8 Supplementary Circuits

To make robust connections between the wires of ESCs and the MCU, a PCB is designed for the ESC pin connections as shown in figure 2.9. Also, among the communication of the

MCUs, multiple wires are used with 1000 ohm resistors. Two PCBs are designed for the communication relay boards (See figure 2.10).

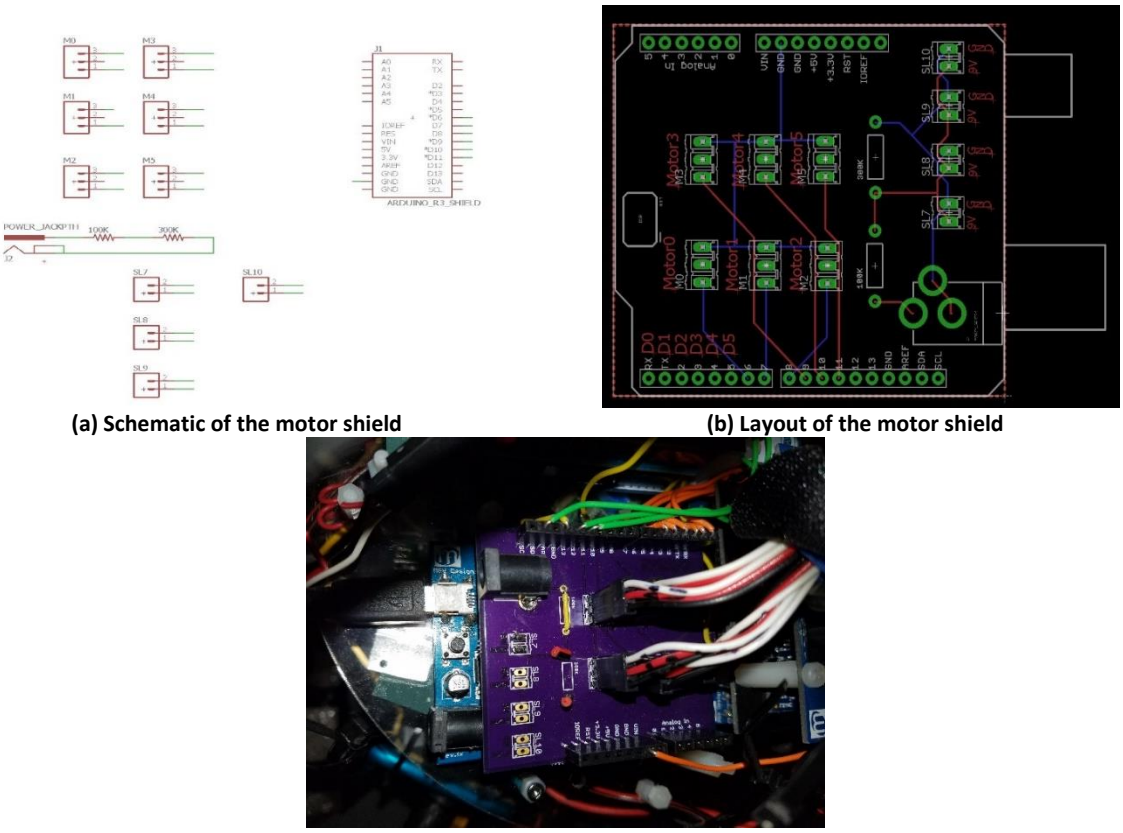

(a) Schematic of the motor shield **(b) Layout of the motor shield**

(c) Printed motor shield circuit

Figure 2.9 Motor shield circuit

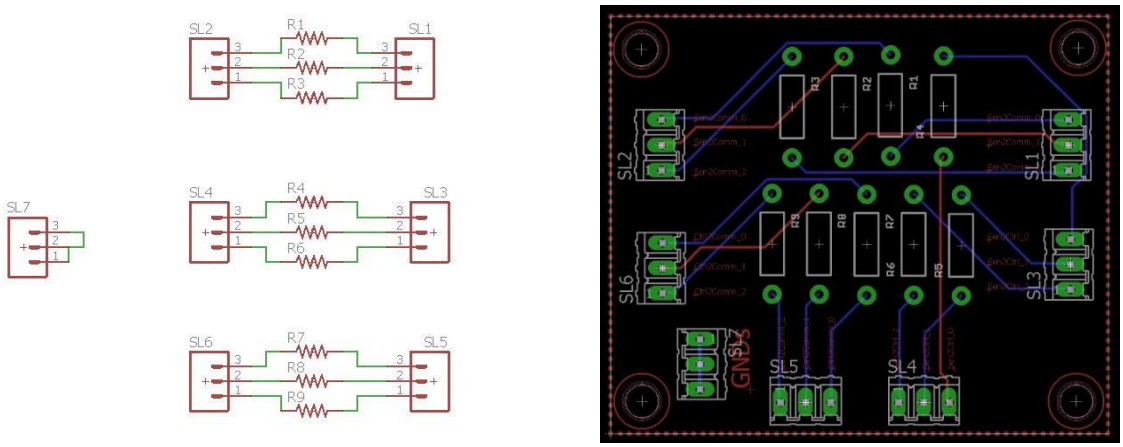

(a) Schematic of the communication relay **(b) Layout of the communication relay**

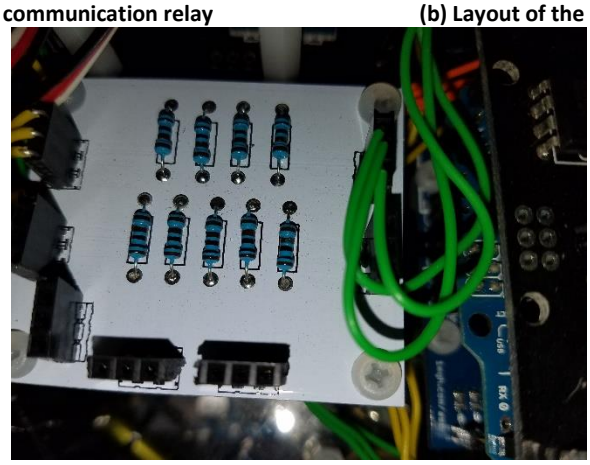

(c) Printed communication relay circuit

Figure 2.10 Communication relay circuit

2.2 Software

For this project, an indoor UAS has been developed. The system is comprised of the vehicle, object/operator, and ground control software (GCS). The INS has an FMC, IMU, and vision (position) sensor. C# and Parallax Spin languages are used for FMC and IMU algorithms respectively. For the GCS, C# application has been written. The GCS can monitor onboard data as well as sending commands and direct control inputs.

2.2.1 Onboard Computers

The INS comprises the four MCUs and the inertial sensors. The first MCU with the inertial sensors is the IMU, which implements complementary filter routines and outputs Euler angles. The second MCU implements PID controller routines and outputs pulse width modulation (PWM) for the ESC. The third MCU collects all the information from the first and second MCUs and reports messages to the GCS via radio transmitter, Xbee, as well as receiving information from the GCS. Finally, the forth MCU receives the 3D relative local coordinates of the target and performs the rotation of the coordinate.

The FMC has C# codes that process RGB and infrared depth frames to estimate the relative local coordinate of a target. Microsoft Kinect SDK 1.7 is used as a Kinect driver to control the circuits of the device. EmguCV is exploited for color detection. Like OpenCV, EmguCV is an open source library for real-time computer vision [34, 35]. Indeed, EmguCV is a .Net wrapper for OpenCV. Also, the C# software is capable of recognizing human gestures using an artificial neural network. Eventually, the FMC can manage the flight mode such as taking-off or landing by the operator's motion input. The detailed algorithm for color detection is discussed in Chapter 4.

2.3 Ground Control Station and Laboratory Environment

2.3.1 Ground Control Station

A ground control software (GCS) is developed in C#. The GCS is capable of monitoring states of the vehicle as well as sending command inputs. Also, the GCS can receive reference

angle for attitude controller from a joystick. The detailed implementation about GCS is discussed in chapter 6.

Figure 2.11 Ground control station

2.3.2 Laboratory Environment

For the safe development of the hexacopter, a safety harness is set up. A climbing rope is connected via a pulley on the ceiling. The rope is fixed on a wall as shown in figure 2.12. Also, the project use the black box method to adjust proportional integral derivative (PID) controller for both attitude and position controller. Therefore, the PID gains are experimentally adjusted. Especially, the attitude controller adjustment process require a testing bed to avoid structural damage as shown in figure 2.13.

Figure 2.12 Safety harness

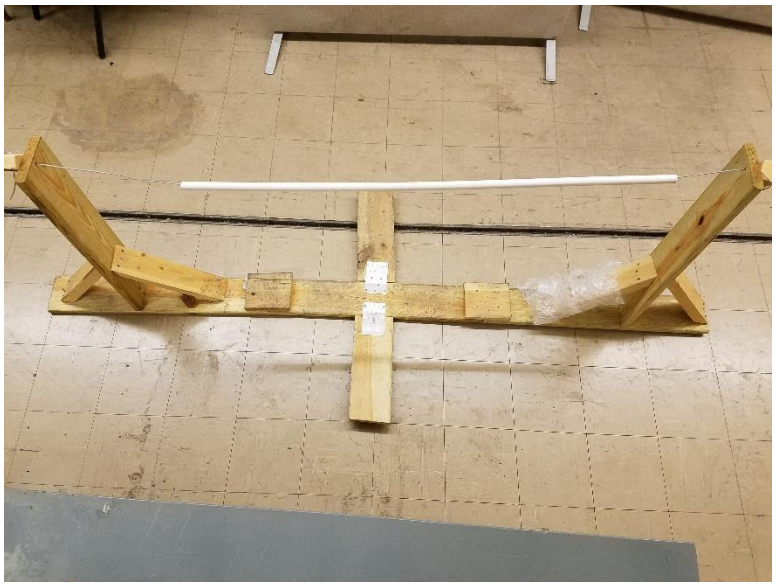

Figure 2.13 Attitude control testing bed

Chapter 3. Inertial Measurement Unit

3.1 Overview

In this chapter, development methods for the inertial measurement unit (IMU) is presented. First, the traditional coordinate systems and rotation matrix are defined. Second, characters and behaviors of the inertial sensors are discussed. Third, the complementary filter (CF) algorithm using the sensors based on the coordinate system is presented. Lastly, the detailed discussion regarding implementation of the algorithm on a microcontroller is discussed.

3.2 Coordinate Systems and Rotation Matrix

The coordinate system used by Schmidt is employed in this project. As shown in the figure 3.1a, the frame E, the earth frame, is fixed at a point on the earth's surface [36]. X_E axis is directed north, Y_E is directed to east, and Z_E is directed to the ground. Also, the frame B, the body frame, moves with a vehicle. X_B is fixed to vehicle X axis. In body frame, figure 3.1b, X axis is fixed to the front side of the vehicle, Y axis is fixed to the right side of the vehicle, and Z axis directs to the bottom of the vehicle. Also, the rotation in terms of X, Y, and Z axes are defined as $\omega_x, \omega_y, and\ \omega_z$ respectively.

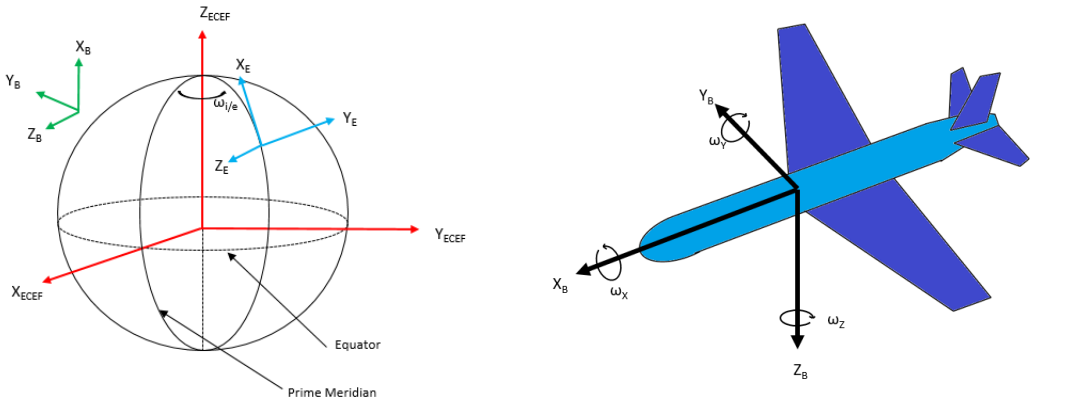

(a) Earth and body coordinate frames (b) Body frame axis, view from the top left of the vehicle

Figure 3.1: Coordinate frame system

Since the hexacopter is assumed as a rigid body and its rotation occurs in three dimensional space, Euler's rotation theorem can be used to relate the rotation between the two frames [36, 37]. As shown in figure 3.2a-c, the Euler angles are defined as $\phi, \theta, and\ \psi$ or roll, pitch, and yaw to relate Frame 1 to 2, Frame 2 to 3, and Frame 3 to 4 respectively.

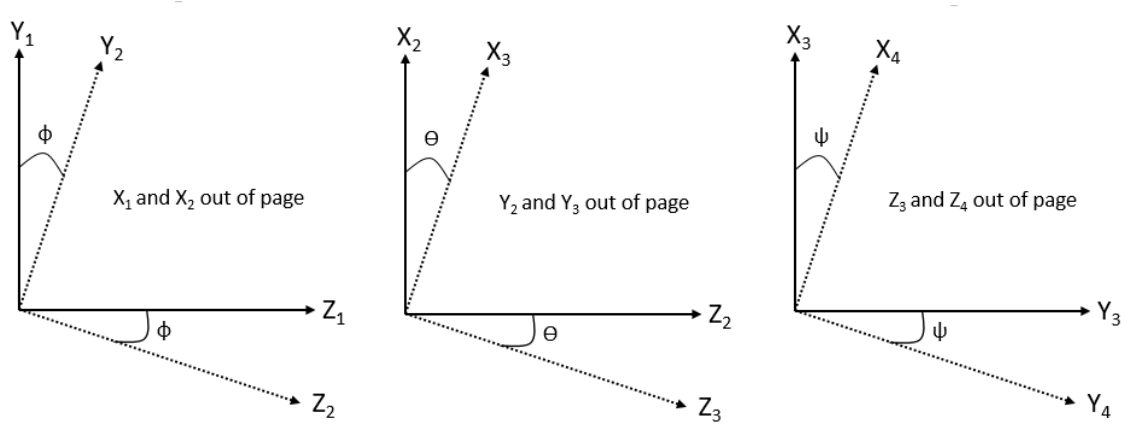

(a) Rotation with respect to X axis (b) Rotation with respect to Y axis (c) Rotation with respect to Z axis

Figure 3.2: Euler angles and rotation

Equations 3.1 - 3.3 show the direction cosine matrix to Figure 3.2a - 3.2c.

$$\begin{bmatrix} X_2 \\ Y_2 \\ Z_2 \end{bmatrix} = \begin{bmatrix} 1 & 0 & 0 \\ 0 & cos(\phi) & sin(\phi) \\ 0 & -sin(\phi) & \cos(\phi) \end{bmatrix} \begin{bmatrix} X_1 \\ Y_1 \\ Z_1 \end{bmatrix} = R_x^T \begin{bmatrix} X_1 \\ Y_1 \\ Z_1 \end{bmatrix} \quad (3.1)$$

$$\begin{bmatrix} X_3 \\ Y_3 \\ Z_3 \end{bmatrix} = \begin{bmatrix} \cos(\theta) & 0 & -\sin(\theta) \\ 0 & 1 & 0 \\ \sin(\theta) & 0 & cos(\theta) \end{bmatrix} \begin{bmatrix} X_2 \\ Y_2 \\ Z_2 \end{bmatrix} = R_y^T \begin{bmatrix} X_2 \\ Y_2 \\ Z_2 \end{bmatrix} \tag{3.2}$$

$$\begin{bmatrix} X_4 \\ Y_4 \\ Z_4 \end{bmatrix} = \begin{bmatrix} \cos(\psi) & \sin(\psi) & 0 \\ -\sin(\psi) & \cos(\psi) & 0 \\ 0 & 0 & 1 \end{bmatrix} \begin{bmatrix} X_3 \\ Y_3 \\ Z_3 \end{bmatrix} = R_x^T \begin{bmatrix} X_3 \\ Y_3 \\ Z_3 \end{bmatrix} \tag{3.3}$$

In general, the direction cosine matrix is the orthogonal matrix, the inverse is the same as transpose. Therefore, to calculate the rotation from Frame 1 to the Frame 2, the transpose of the matrixes can relate the two frames as shown in equation 3.4.

$$\begin{bmatrix} X_1 \\ Y_1 \\ Z_1 \end{bmatrix} = \begin{bmatrix} 1 & 0 & 0 \\ 0 & cos(\phi) & -sin(\phi) \\ 0 & sin(\phi) & \cos(\phi) \end{bmatrix} \begin{bmatrix} X_2 \\ Y_2 \\ Z_2 \end{bmatrix} = R_x \begin{bmatrix} X_2 \\ Y_2 \\ Z_2 \end{bmatrix} \tag{3.4}$$

Similarly,

$$\mathrm{R}_y = \begin{bmatrix} \cos(\theta) & 0 & \sin(\theta) \\ 0 & 1 & 0 \\ -\sin(\theta) & 0 & cos(\theta) \end{bmatrix} \tag{3.5}$$

$$\mathrm{R}_z = \begin{bmatrix} \cos(\psi) & -\sin(\psi) & 0 \\ \sin(\psi) & \cos(\psi) & 0 \\ 0 & 0 & 1 \end{bmatrix} \tag{3.6}$$

Therefore, to represents the Frame 4 to Frame 1, the rotation matrix can be computed as below equation 3.7.

$$\mathrm{R}_{\mathrm{zyx}} = R_z R_y R_x \tag{3.7}$$

$$= \begin{bmatrix} cos(\theta)\, cos(\psi) & sin(\phi)\cos(\theta) - cos(\phi)\, sin(\psi) & cos(\phi)\sin(\theta)\cos(\psi) + sin(\phi)\, sin(\psi) \\ cos(\theta)\, sin(\psi) & sin(\phi)\cos(\theta)\sin(\psi) + cos(\theta)\, cos(\psi) & cos(\phi)\sin(\theta)\sin(\psi) - sin(\phi)\, cos(\psi) \\ -sin(\theta) & sin(\theta) cos(\theta) & cos(\phi) cos(\theta) \end{bmatrix}$$

Using this, the vector relations in ground-body frames can be simply represented.

$$V_{earth} = R \times V_{body} \tag{3.8}$$

where

- $\mathrm{V}_{\mathrm{earth}}$ is a vector in the ground/earth frame,

- $\mathrm{V_{body}}$ is a vector in the body frame, and
- R is the $\mathrm{R_{xyz}}$ from equation 3.7

3.3 Inertial Sensors

3.3.1 Gyroscope and Accelerometer

A three degree of freedom (DOF) gyroscope provides angular velocities for x, y, and z axes. For this project, the sensitivity of the gyroscope in MPU9150 board is set to $\pm 250\ ^\circ/s$. By integrating the angular rotation, the Euler angle can be estimated.

$$\begin{bmatrix}\phi\\ \theta\\ \psi\end{bmatrix}_{i+1} = \begin{bmatrix}\phi\\ \theta\\ \psi\end{bmatrix}_{i} + \begin{bmatrix}\omega_x\\ \omega_y\\ \omega_z\end{bmatrix}_{i} \times \Delta t \tag{3.9}$$

where

- i+1 is the next state, and
- i indicates the current state

A three DOF accelerometer provides acceleration on the body. For this project, the sensitivity is set to $\pm 2g$, where g is the gravitational acceleration. During steady flight without external disturbance, roll and pitch angles can be estimated.

$$\begin{bmatrix}\phi\\ \theta\\ \psi\end{bmatrix}_{i} = \begin{bmatrix}\tan^{-1}\frac{g_x}{\sqrt{g_y^2+g_z^2}}\\ \tan^{-1}\frac{g_y}{g_z}\\ 0\end{bmatrix}_{i} \tag{3.10}$$

However, the equation 3.8 and 3.9 do not consider the noise of the sensor and the accelerations on the rigid body. Without estimating the noise and acceleration due to inertial force, the result can be misleading. Figure 3.3 shows roll estimation in x, y, z axes using equation 3.8 and 3.9. As indicated, the equations cannot precisely estimate the attitude of the vehicle because the

gyroscope noise is sampled around 35th data point and the integration accumulated it. As a result, although there was no rotation, gyroscope-based roll angle estimation drifted significantly. The detailed algorithm to compensate the drift is discussed in chapter 3.4.

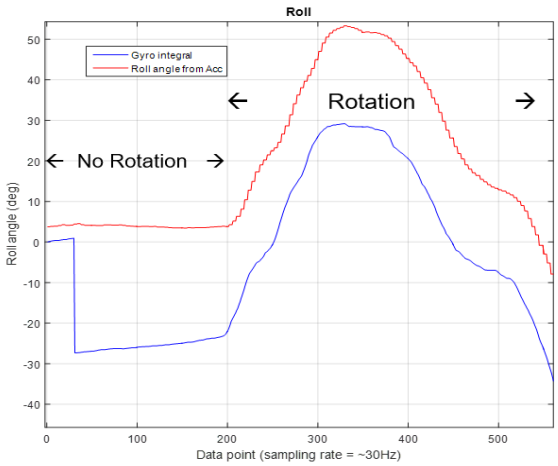

Figure 3.3 Roll angle estimation, integration only

3.3.2 Magnetometer

Three DOF magnetometer measures Earth magnetic fields. Since both gyroscope and accelerometer are not capable of providing heading estimation, a magnetometer is used to provide heading information. There is an issue to be addressed for the reliable estimation of heading. The magnetometer's raw data is decentered due to a bias as shown in Figure 3.4. The bias is the result of local magnetic field varying by the given environment for the installation and operation of the vehicle [38]. Yet, once the sensor is calibrated, the variation during flight is small [38].

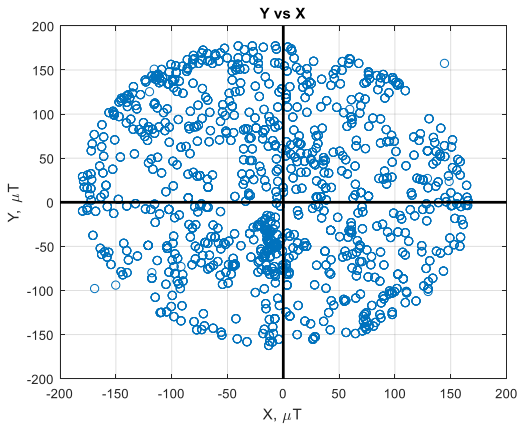

(a) Raw magnetometer value Y vs X

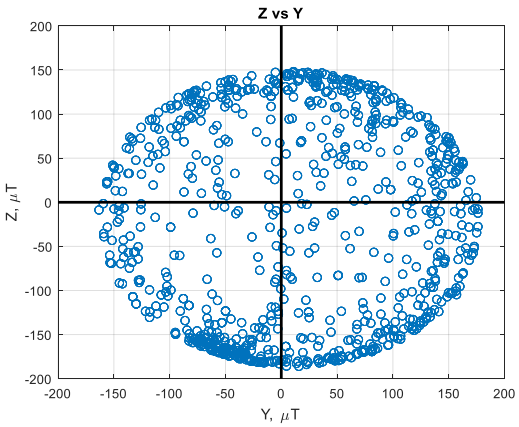

(b) Raw magnetometer value Z vs Y

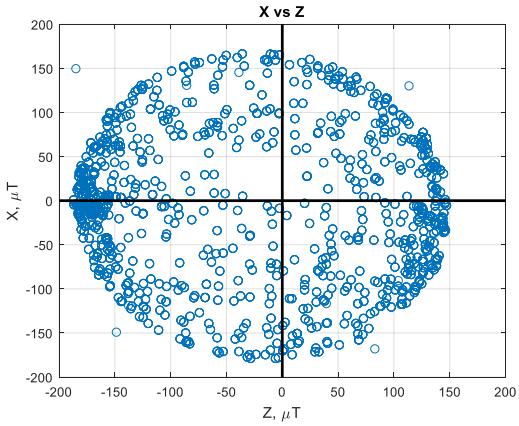

(c) Raw magnetometer value X vs Z

Figure 3.4 Raw magnetometer value distribution

To re-centralize, max and min values are selected from each axis, and their mean value is calculated since the mean value indicates the magnitude of the off-center. For the plots presented here, the offset is computed as 9, -167, and 23 for x, y, and z axis each as shown in figure 3.5.

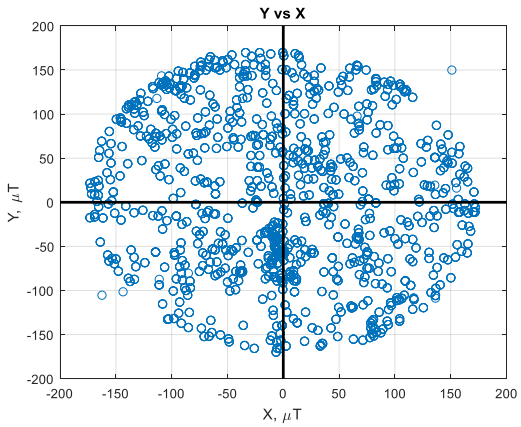

(a) Corrected magnetometer value Y vs X

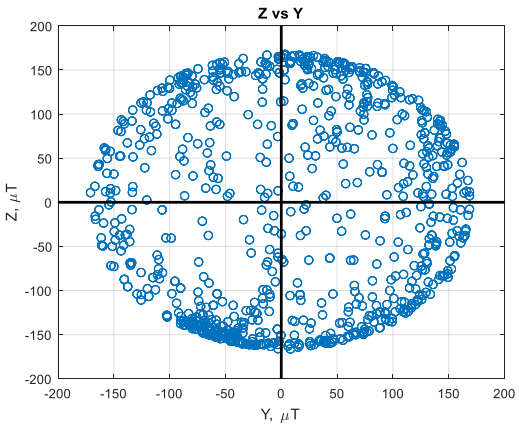

(b) Corrected magnetometer value Z vs Y

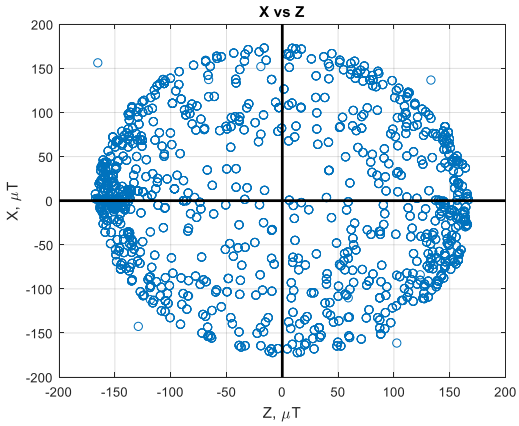

(c) Corrected magnetometer value X vs Z

Figure 3.5 Corrected magnetometer value distribution

3.4 Complementary Filter

As noted in chapter 3.3, the immediate use of raw values of the sensor does not provide a robust and consistent estimation of the vehicle state. To achieve robust estimation, a complementary filter using the rotation matrix is employed in this project [37]. The rotation matrix provides reliable estimation than equations 3.1 and 3.2 since the estimation is based on angular velocity while the error can be corrected by using the acceleration and heading.

3.4.1 Rotation Matrix Construction

Assuming that the body is resting on the ground at the begging, rotation matrix can be initialized using equations 3.7 and 3.8 since the three equations output $\phi, \theta, and\ \psi$.

$$[R]_i = \begin{bmatrix} \cos(\theta)\cos(\psi) & \sin(\phi)\cos(\theta) - \cos(\phi)\sin(\psi) & \cos(\phi)\sin(\theta)\cos(\psi) + \sin(\phi)\sin(\psi) \\ \cos(\theta)\sin(\psi) & \sin(\phi)\cos(\theta)\sin(\psi) + \cos(\theta)\cos(\psi) & \cos(\phi)\sin(\theta)\sin(\psi) - \sin(\phi)\cos(\psi) \\ -\sin(\theta) & \sin(\theta)\cos(\theta) & \cos(\phi)\cos(\theta) \end{bmatrix}$$

After establishing initial rotation matrix, next rotation matrix can be constructed by using angular velocities from the gyroscope.

$$[R]_{i+1} = [R]_i \left([I] + \begin{bmatrix} 0 & -\omega_z & \omega_y \\ \omega_z & 0 & \omega_x \\ -\omega_y & -\omega_x & 0 \end{bmatrix}_i \times \Delta t \right) \tag{3.11}$$

where

- $[I]$ is identity matrix.

Since the raw values of angular velocity from the gyroscope do not conserve orthogonality, the rotation matrix does not conserve orthogonality as well. Therefore, the correction for preserving orthogonality needs to be addressed. The following equations correct orthogonality since the rotation matrix is symmetric and orthogonal.

$$E = [R_1]^T [R_2] \tag{3.12}$$

where

- E is orthogonality error,
- $[R_1]$ is the first column of $[R]_{i,\ earth}$, and
- $[R_2]$ is the second column of $[R]_{i,\ earth}$

Since the error is calculated by dot product of first two columns, error can be equality divided and subtracted to each column vectors.

$$[R_1]_{orth} = [R_1] - \frac{E}{2}[R_2] \tag{3.13}$$

$$[R_2]_{orth} = [R_2] - \frac{E}{2}[R_1] \tag{3.14}$$

where

- $[R_1]_{orth}$ is the orthogonalized vector of the first column of $[R]_{i,\ earth}$, and
- $[R]_{orth}$ is the orthogonalized vector of the second $[R]_{i,\ earth}$

Since the rotation matrix has to keep orthogonality for all axes, the third column of $[R]_{i,\ earth}$ can be calculated by using cross product of first two orthogonalized column vectors.

$$[R_3]_{orth} = [R_1]_{orth} \times [R_2]_{orth} \tag{3.15}$$

As a result, $[R]$ can be expressed as below.

$$[R]_{orth} = \ [\ [R_1]_{orth} \quad [R_2]_{orth} \quad [R_3]_{orth}\ ] \tag{3.16}$$

Finally, each row of the rotation matrix needs to be scaled to one. Since magnitude of each row does not significantly vary from one, Taylor expansion can be used to renormalize the rows.

$$[R_1]_{norm} = \frac{1}{2}\left(3 - [R_1]_{orth} \cdot [R_1]_{orth}\right)[R_1]_{orth} \tag{3.17}$$

$$[R_2]_{norm} = \frac{1}{2}\left(3 - [R_2]_{orth} \cdot [R_2]_{orth}\right)[R_2]_{orth} \tag{3.18}$$

$$[R_3]_{norm} = \frac{1}{2}\left(3 - [R_3]_{orth} \cdot [R_3]_{orth}\right)[R_3]_{orth} \tag{3.19}$$

3.4.2 Error Correction

As indicated earlier, the orthogonalization and the renormalization do not guarantee robust estimation of the rotation since the source values; the angular velocities of three axes have noise. Even though the noise at a point is insignificant, as the integration processes iterate, the error will accumulate, and this can lead to significant amount of drift of the rotation matrix. To be able to estimate vehicle attitude, the drift needs to be corrected. The accelerometer and the magnetometer are used as reference sources for the correction.

Since rotation matrix conserves rotation through the rotation axes, when body frame accelerometer is given, earth frame acceleration should indicate the gravitational acceleration vector, i.e. $[0 \quad 0 \quad -9.81]\, m/s^2$, assuming that the rotation matrix has no error due to the sensor noise. However, often time, the rotated body frame to earth frame acceleration vector is not exactly equal to the gravity vector. By contradiction to the assumption that the rotation matrix is correct, the rotation matrix has error whenever the ground frame acceleration vector is not equal to the gravitational acceleration vector. Using cross product, the magnitude of the error in x and y axes rotation angles between the gravity vector and the ground frame acceleration vector with the drift can be computed.

$$[\mathrm{E_{xy}}] = [\mathrm{ACC_{earth}}] \times [G] \tag{3.20}$$

where

- $[\mathrm{E_{xy}}]$ is the error vector in the ground frame due to the drift and the z component is 0,
- $[\mathrm{ACC_{earth}}]$ is ground frame acceleration, and
- $[\mathrm{G}]$ is gravity vector, [0 0 g], where g = -9.81 $\frac{\mathrm{m}}{\mathrm{s}^2}$

To calculate z component of rotation error regarding ground frame, magnetometer data can be incorporated in a similar manner. Since default heading is set to the North, i.e.$[1 \quad 0 \quad 0]$, ground frame magnetometer should indicate the North. Otherwise, it reveals the error due to the drift of z axis gyroscope value.

$$[\mathrm{E_z}] = [MAG_{earth}] \times [North] \tag{3.21}$$

where

- $[\mathrm{E_z}]$ is z components of error in the ground frame due to drift,
- $[\mathrm{MAG_{earth}}]$ is ground frame heading, and
- $[\mathrm{North}]$ is heading vector for the North, [1 0 0].

By adding the two error vectors in ground frame, the total error vector in ground frame perspective can be constructed and rotated back to the body frame for the correction.

$$[\mathrm{E}]_{\mathrm{earth}} = \left[E_{xy}\right] + [E_z]$$

$$[\mathrm{E}]_{\mathrm{body}} = [R']_{norm}\,[E]_{body} \tag{3.22}$$

Eventually, the error information is fed for proportional integral (PI) compensator by constructing a new rotation matrix based on the error.

$$[\mathrm{R}]_{\mathrm{cor}} = [R']_{norm}\,([I] + \begin{bmatrix} 0 & E_z & -E_y \\ -E_z & 0 & E_x \\ E_y & -E_x & 0 \end{bmatrix} \times K_p) \tag{3.23}$$

where

- $[\mathrm{R}]_{\mathrm{cor}}$ is corrected rotation matrix,
- $\mathrm{E_x}$ is x element of the body frame error vector,
- $\mathrm{E_y}$ is y element of the body frame error vector,
- $\mathrm{E_z}$ is z element of the body frame vector, and
- $\mathrm{K_p}$ is the proportional gain of PI compensator.

Also, to prevent further error due to gyroscope bias, error integration can be considered by accumulating the error and subtracting it for the next iteration.

$$[\mathrm{E}]_{\mathrm{acc}} = [E]_{acc} + K_i\,[E]_{body} \tag{3.24}$$

$$\begin{bmatrix} \omega_x \\ \omega_y \\ \omega_z \end{bmatrix} = \begin{bmatrix} \omega_{x,\ raw} \\ \omega_{y,\ raw} \\ \omega_{z,\ raw} \end{bmatrix} - [E]_{acc} \tag{3.25}$$

where

- $[\mathrm{E}]_{\mathrm{acc}}$ is accumulated error in the body frame, and
- $\mathrm{K_i}$ is integral gain of the PI compensator.

3.5 Results

3.5.1 Simulation Result

Figures 3.6-3.8 show the Matlab-based CF algorithm results.

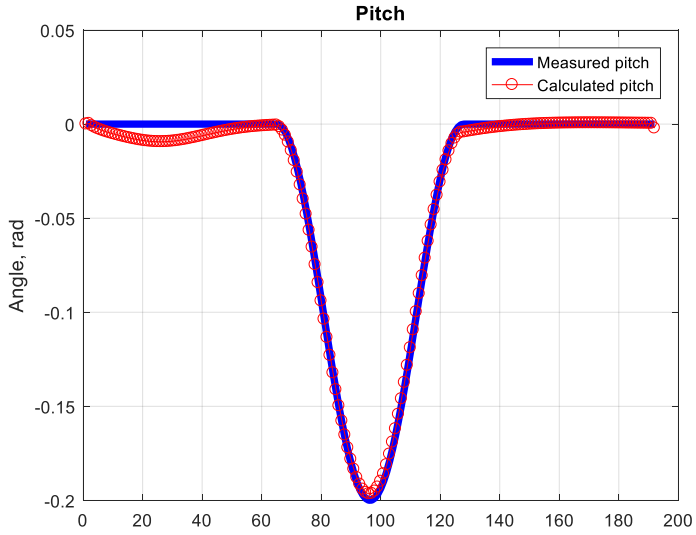

Figure 3.6 CF estimation of pitch, simulation output

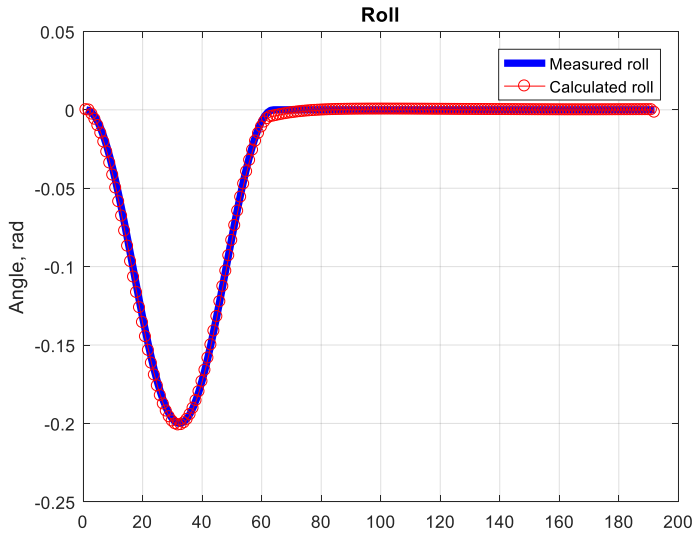

Figure 3.7 CF estimation of roll, simulation output

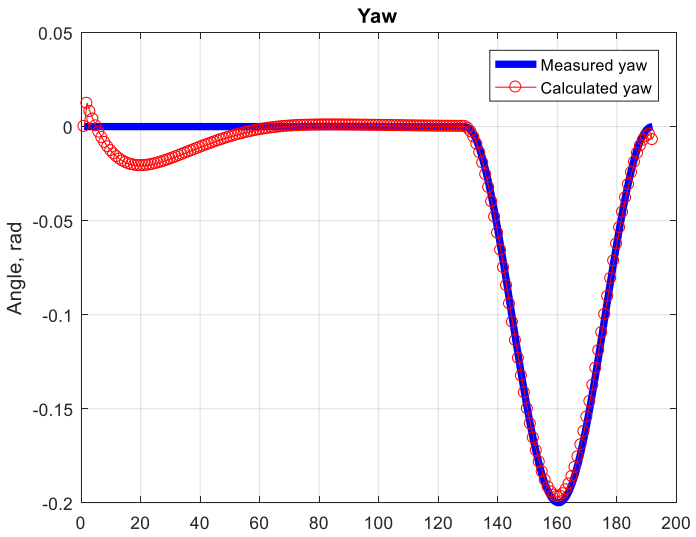

Figure 3.8 CF estimation of yaw, simulation output

3.5.2 Implementation

In this section, how the above algorithm has been implemented on the IMU is discussed. Since the sampling rates of the sensors are different, four cogs of the MCU have been exploited to process the CF routines while preserving the original sampling rates of the sensors. Also, to share the memory space with other MCUs, three cogs are used as shown in figure 3.9.

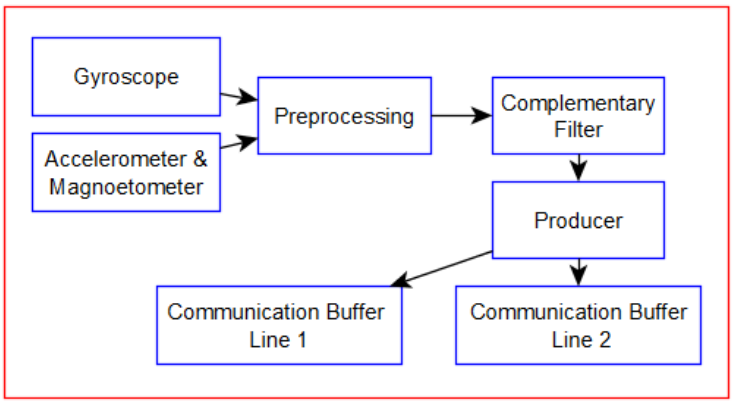

Figure 3.9 IMU Structure

To read each sensor, I2C protocol is used. Although I2C protocol allows the line to read several sensors, the sampling rate decreases since several sensors are using the communication lines. By using different cogs, the sampling rates for the CF algorithm are 175 Hz for the gyroscope, 130 Hz for the accelerometer, and 10 Hz for the magnetometer.

Preprocessing is required since the raw magnetometer values contain noise, which can result in uncertainties in estimation as shown in figure 3.10 [38]. Similarly, the accelerometer values go through an average filter, which outputs the average value of the data at 13Hz as shown in figure 3.11.

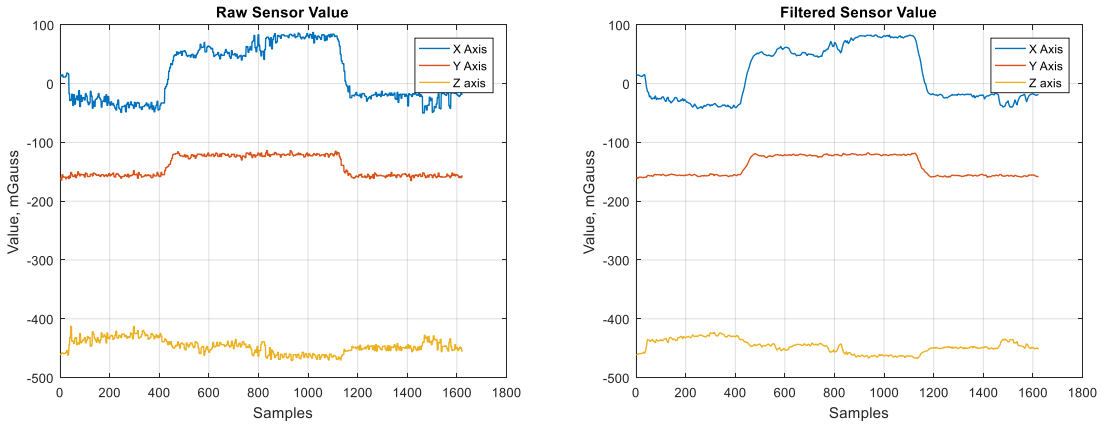

(a) Raw magnetometer signals

(b) Low pass filtered magnetometer signals

Figure 3.10 Magnetometer signals

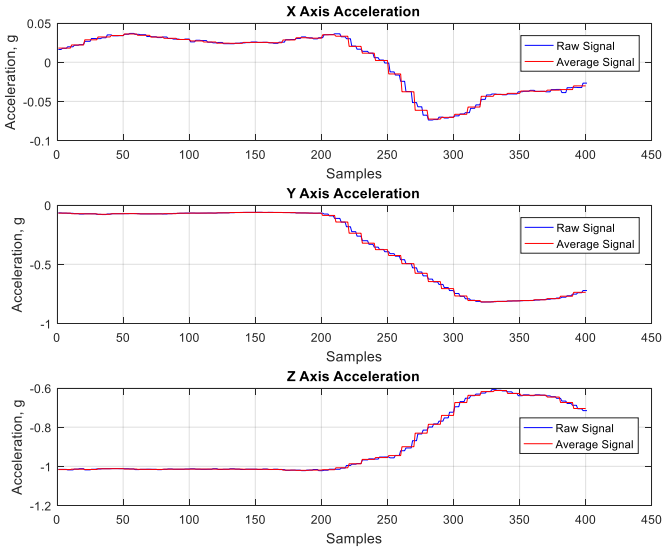

Figure 3.11 Average filtered accelerometer signals

Since the CF routine is the last part processed in the algorithm, previous data such as raw signals are encapsulated by the tiers. Encapsulation reduces the complexity of the algorithm by revealing only necessary data to the upper layer. As shown in figure 3.12, Tier 1 reads the raw sensor data and adjusts the axis convention so that the axes can be aligned with the axis convention discussed in chapter 3.2. In Tier2, the signals are filtered. Lastly, the CF algorithm is implemented in Tier3.

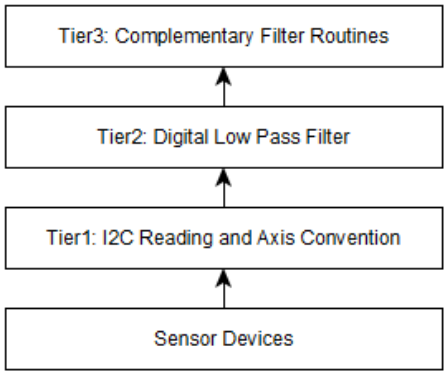

Figure 3.12 Tiers of CF IMU structure

3.5.3 Experimental Result

In this section, the IMU data output is presented. The same CF algorithm is used as chapter 3.5.1. The only difference is that Parallax Propeller MCU does not support primitive floating point types. To conserve the computing speed, 32 bit signed long type variables are exclusively used. Figures 3.13 – 3.15 show the results from MCU implementation. The output of the CF (green line) at each axis shows that Euler angle estimation has less noise and drift with negligible phase shift.

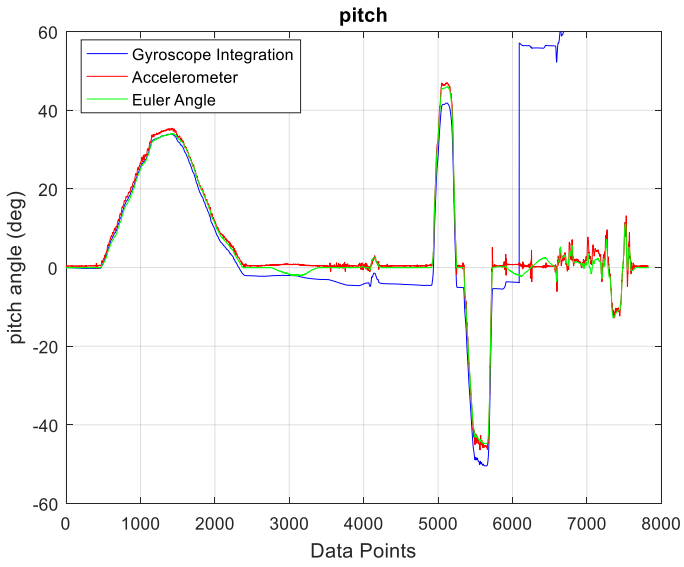

Figure 3.13 CF estimation of pitch, IMU output

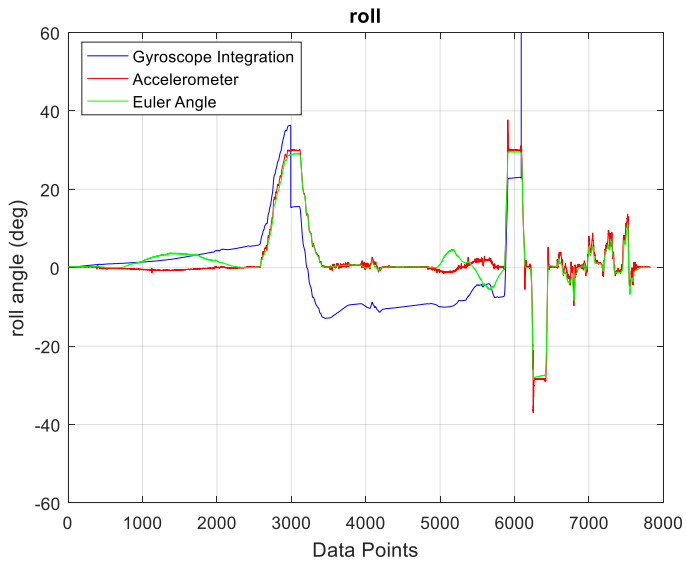

Figure 3.14 CF estimation of roll, IMU output

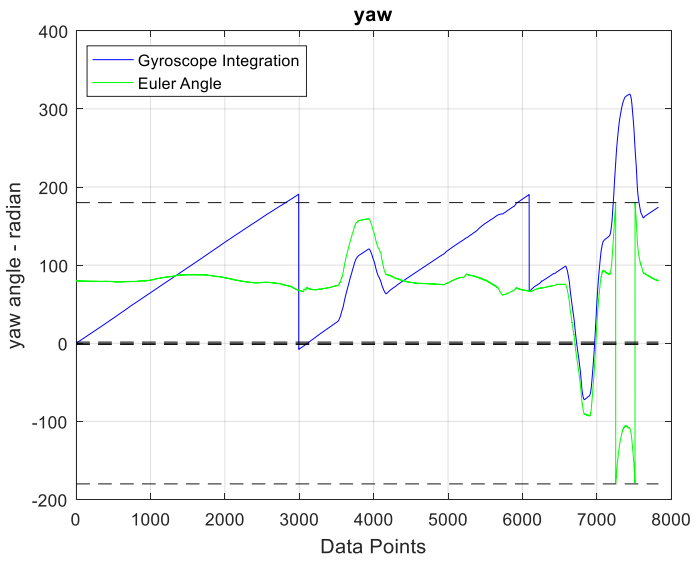

Figure 3.15 CF estimation of yaw, IMU output

Chapter 4. Vision Sensor and Flight Management Computer

4.1 Color Tracking

In this chapter, object and body tracking methods are discussed. Microsoft Kinect is a camera mounted onboard. The camera provides 30 fps RGB, infrared, depth, and skeletal frames. Tracking a target or estimating relative coordinates of the target is an important process for the drone to navigate in the GPS-denied situation. For this system, a set of computer vision algorithms is exclusively applied as a surrogate position estimator. To aid taking off, landing, or navigation, a color detection algorithm is implemented using Microsoft Kinect SDK 1.7 (MSKSDK) and EmguCV [39]. The color detection algorithm uses RGB and depth frames to estimate the 3D coordinate of a red object. Figure 4.1 shows the flow of the color detection routines. The routines in green are presented in the following sections and INS part is discussed in Chapter 5.

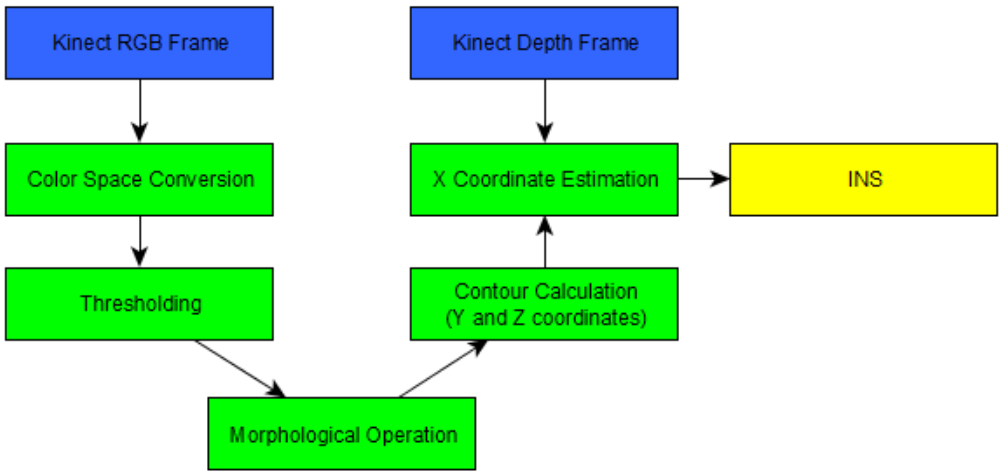

Figure 4.1 Color detection routines

4.1.1 Color Space Conversion

The MSKSDK can output an RGB frame in bitmap format using a byte array. OpenCV then creates an RGB image matrix. However, RGB frame can be misleading because RGB color space is nonlinear [40]. Especially, brightness change in the RGB space results in having different hues. The light intensity varies by the angle and the position of the camera. During the drone operation, the onboard camera is exposed to the structural vibration, attitude noise, and continuously changing position. Therefore, for the robustness of the color detection algorithm, RGB color space needs to be converted to hue-saturation-value (HSV) color space. With HSV frame, thresholding can be operated regardless of change of light intensity. In HSV frame, hue is the type of color, saturation is the chroma, and value represents the brightness as shown in Figure 4.3. Therefore, HSV frame provides abundant information regarding the pixels in the frame.

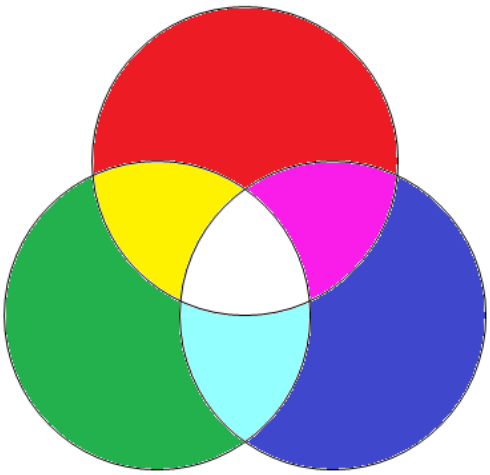

Figure 4.2 RGB Color Space

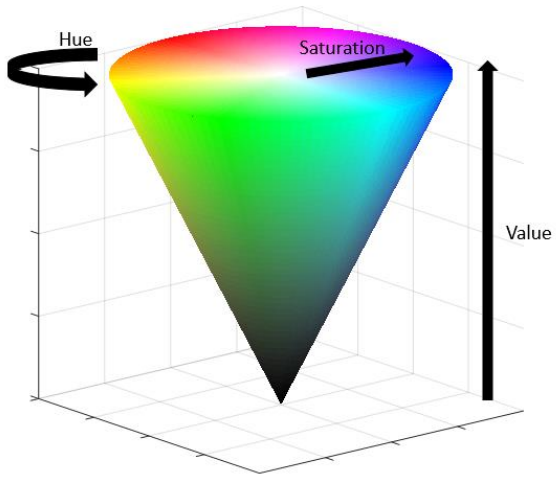

Figure 4.3 HSV Color Space

In EmguCV, CvInvoke.cvtColor(InputArray src, OutputArray dst, int code) function is used to convert the color space. The first argument is the RBG image array and the second one is the empty array that will contain the converted HSV image. The last argument of the function, "code", is ColorConversion enumerator. In this case, ColorConversion.Rgb2Hsv is passed. Figure 4.4 illustrate the color space conversion. In figure 4.4 (a), 10% of the noise is artificially added to emualte noisy flight environment.

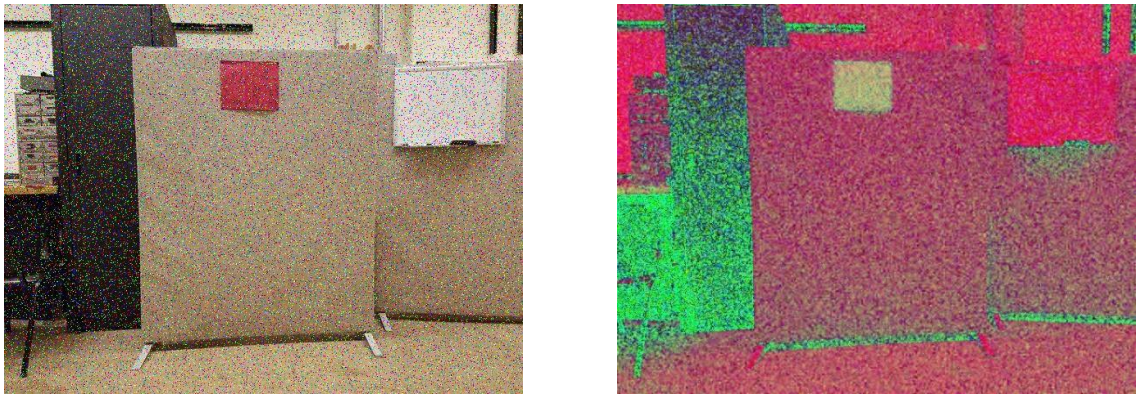

(a) Noisy Image in RGB color space (b) Converted image in HSV color space

Figure 4.4 RGB (a) and HSV (b) images

4.1.2 Thresholding

The “red” pixels in RGB frame are converted to the certain ranges of literals in the HSV frame. The red hue value is around 160 – 179 [39]. The saturation and the brightness are adjusted experimentally since they differ by the environments. To detect the pixels of the object of interest, in this case, red, thresholding routines are processed. The thresholding is process on the each axis of the HSV frame. For the hue axis, the values between 110 and 160 are passed at the specific lab environment for the red pixels. The passed pixels are represented by 1 or 0 otherwise as shown in figure 4.5. Similarly, the saturation and value frames are thresholded as figures 4.6 - 4.7 show.

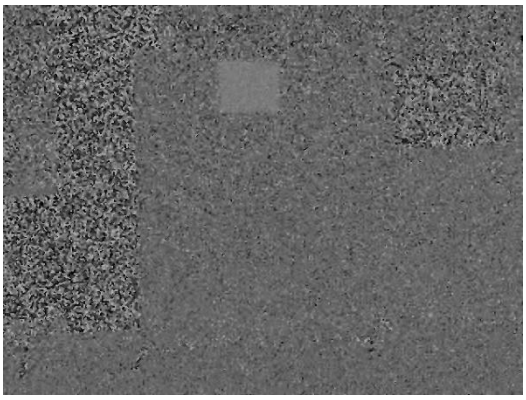

(a) Hue frame

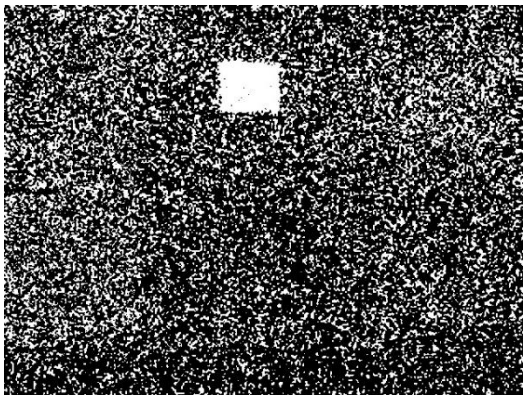

(b) Thresholded hue frame

Figure 4.5 Hue frame filter

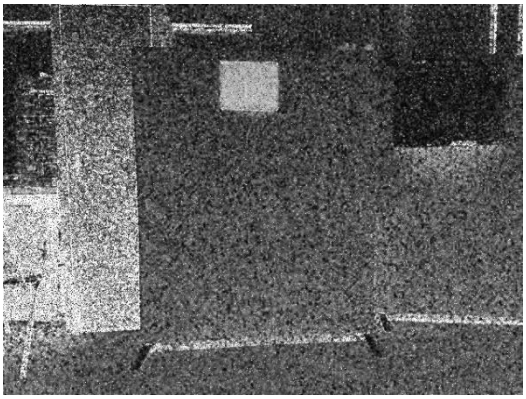

(a) Saturation frame

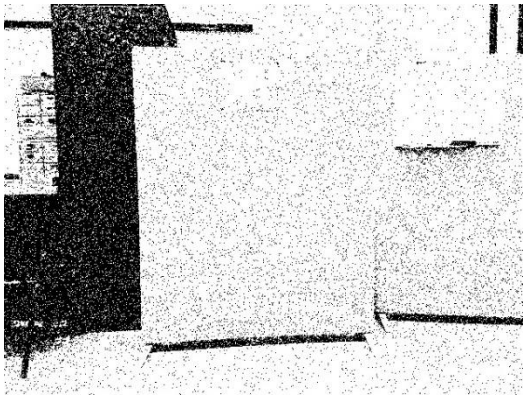

(b) Thresholded saturation frame

Figure 4.6 Saturation frame filter

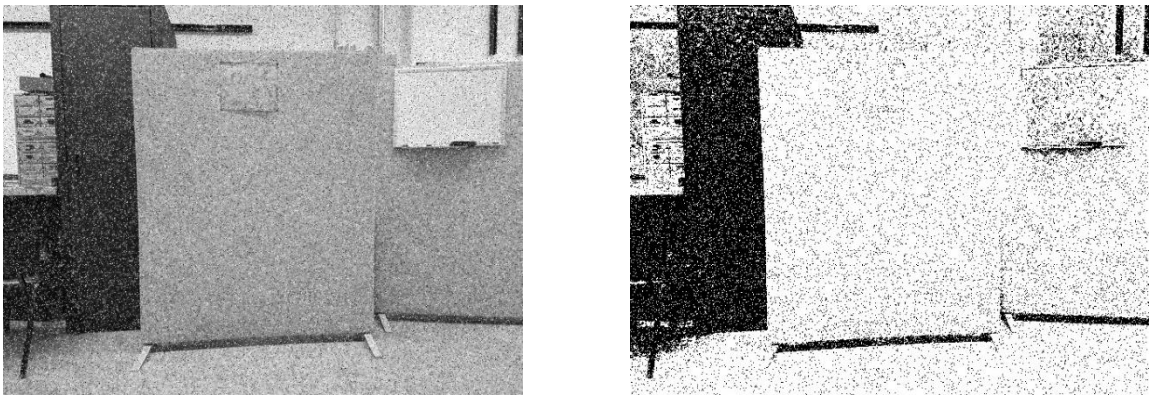

(a) Value frame (b) Thresholded value frame

Figure 4.7 Value frame filter

Eventually, the filtered frames are overlapped and their binary pixels are merged by bit-wise AND-gates. Figure 4.5 shows the resultant frame.

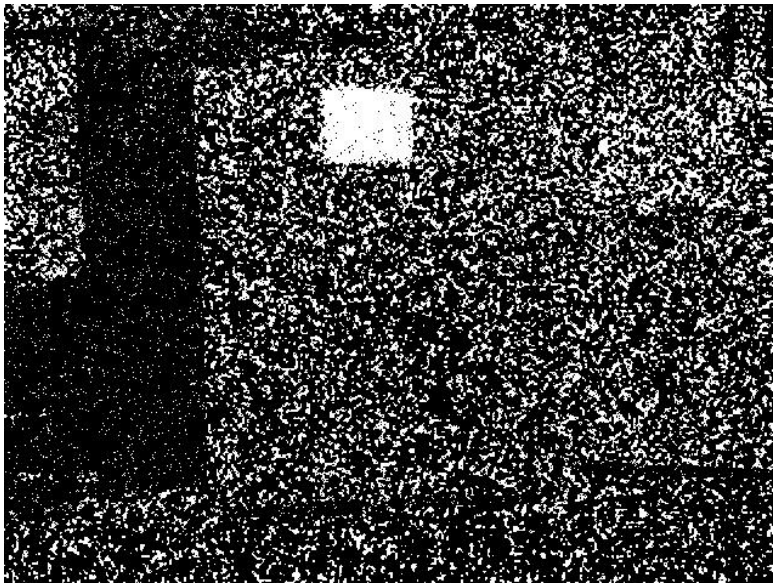

Figure 4.5 AND gated filtered image

4.1.3 Morphological Operation

Since the noise in the resultant frame is significant, the small white dots can be eliminated by morphological opening. Unless the noise are not reduced, the contour algorithm needs lots of computations since the algorithm has to iterate every white pixels in the frame.

Such excessive iterations can end up with the delaying the process. The opening process is morphological erosion followed by dilation. By eroding the pixels, minimal kernels are left [42]. Dilation is the reverse process of erosion. Using EmguCV, CvInvoke.Erode() and CvInvoke.Dilate() are operated. The result frame that morphological opening is process is presented in figure 4.6 (a). Also, to fill the small black holes in the white blob, morphological closing is operated based on the figure 4.6 (a). It is shown in figure 4.6 (b).

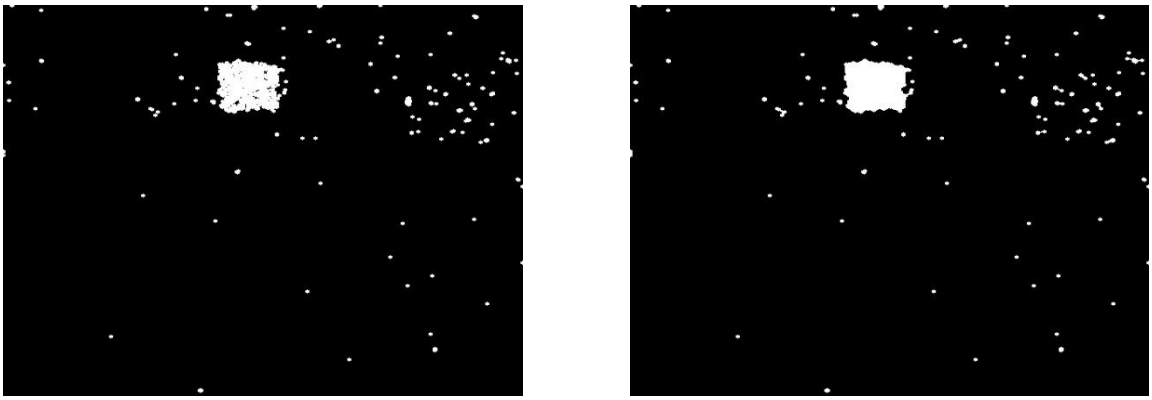

(a) Morphologically opened frame (b) Morphologically closed frame

Figure 4.6 Morphological operations of the frame

4.1.4 Contour and Relative Coordinate Estimation

To locate the largest white blob in figure 4.6, CvInvoke.findContours() is used [34, 35, 43]. The function returns the array of contour information of all white blobs in figure 4.6. The information includes 2D vector position of the contour, width, height, and area. Since the significant white blob's area is usually larger than 500, other small white blobs can be suppressed as shown in figure 4.7.

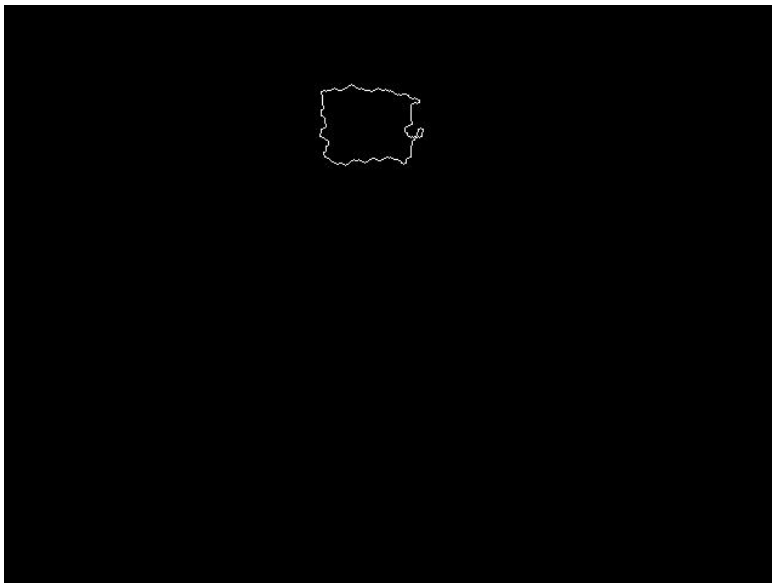

Figure 4.7 The contour of the largest white blob

Using the information provided by CvInvoke.FindContours(), the red object in the input frame can be located as figure 4.8.

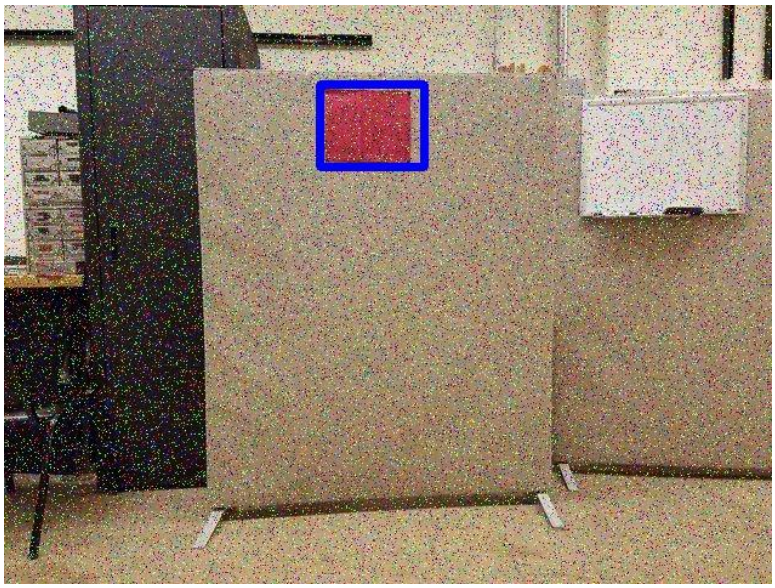

Figure 4.8 Red object detection, marked by a blue rectangle

Based on the 2D coordinate from the RGB frame, the depth, or the X axis coordinate of the object can be calculated using the depth frame from the Kinect. The depth frame has one channel whose values span from 0 to 255. The higher value means the further pixels (see figure

4.9). Although the size of the depth frame is slightly smaller than the RGB frame, the error is negligible when the 2D coordinate of the red object from the RGB frame is overlaid to calculate the depth of the object.

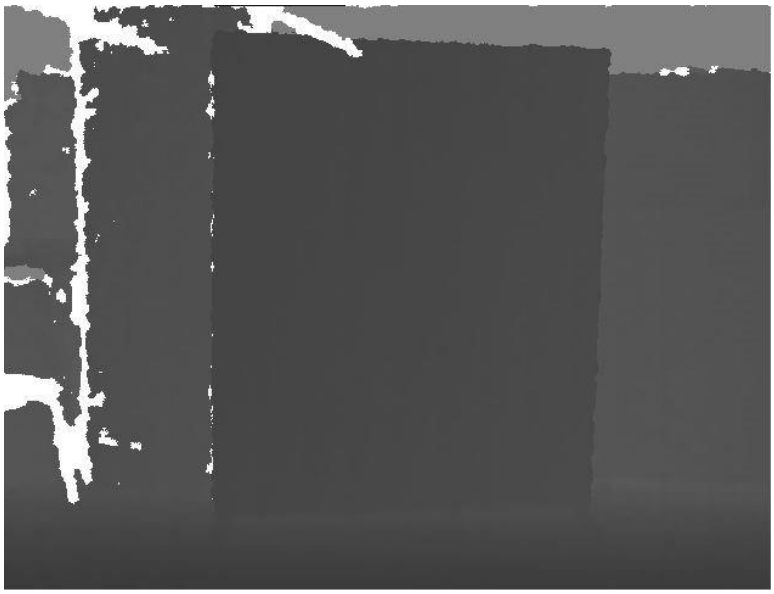

Figure 4.9 Depth frame

The depth is calculated by averaging the pixels in the contour area. Yet, the depth information is not the x coordinate of the object because the depth frame only offers the distance (See figure 4.10) [46]. The calculation of the X coordinate can be simply done by Equation 4.1. However, the y and z coordinate value is in pixel-wise unit while the depth frame can be directly converted to physical unit such as meter. Therefore, the conversion from pixel to real-world unit needs to be processed before the x coordinate calculation.

$$\text{x coordinate} = \sqrt{\text{Distance}^2 - y^2 - z^2} \tag{4.1}$$

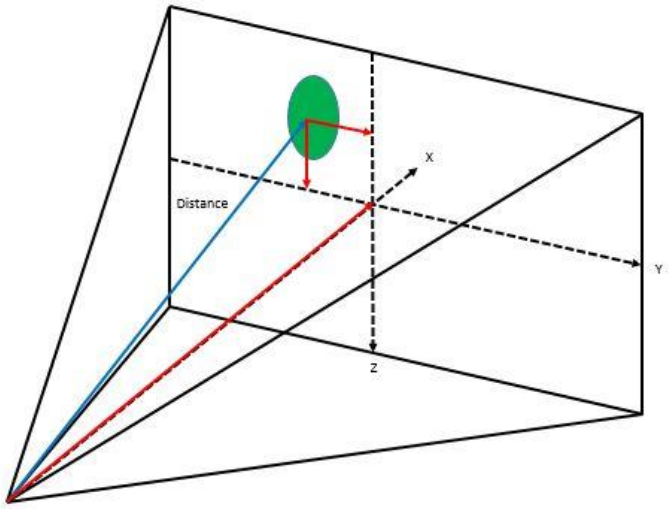

Figure 4.10 3D view of Kinect field of view

The given information so far is shown in figure 4.11. Kinect's horizontal field of view, fov_{hor}, pixel-wise maximum Y coordinate, Y_{max}, distance between the points O and Y, and pixel-wise distance $\overline{XY_{pix}}$ are known. By linearly approximating the relation between $\overline{XY_{pix}}$ and α, the angle to the object from the center, physical world $\overline{XY_{pix}}$ can be approximated using equations 4.2 and 4.3.

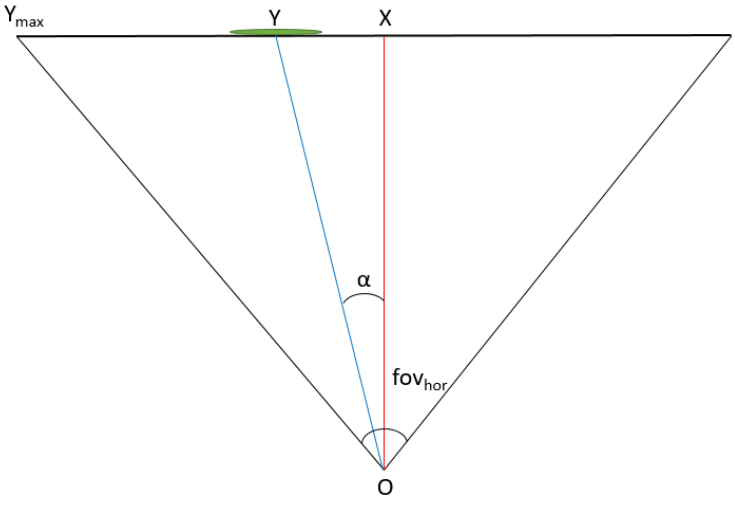

Figure 4.11 Top view of Kinect horizontal field of view

$$\alpha \approx \frac{\overline{XY_{pix}}}{\overline{XY_{max,pix}}} \times \frac{fov_{hor}}{2} \quad (4.2)$$

$$\overline{XY_{phy}} = \sin(\alpha) \times \overline{OY_{phy}} \quad (4.3)$$

where

- fov_{hor} is 62 degree [44] and
- the frame size in pixel is 640 by 480 (width by height).

Since the maximum depth that Kinect can sense is 3 meters, the maximum possible error of the X coordinate due to linear approximation using equations 4.1 - 4.3 is approximately 5 cm. Z coordinate conversion can be done in the same manner. 49 degree is used for the vertical field of view [44].

4.2 Body Part Detection

MSKSDK offers body parts' 3D coordinates. Figure 4.12 shows types of the body parts available in MSKSDK. Since the coordinate system is different from the definition in chapter 3, the axes need to be changed correspondingly. In this project, left and right hand and spine coordinates are used for the simplicity.

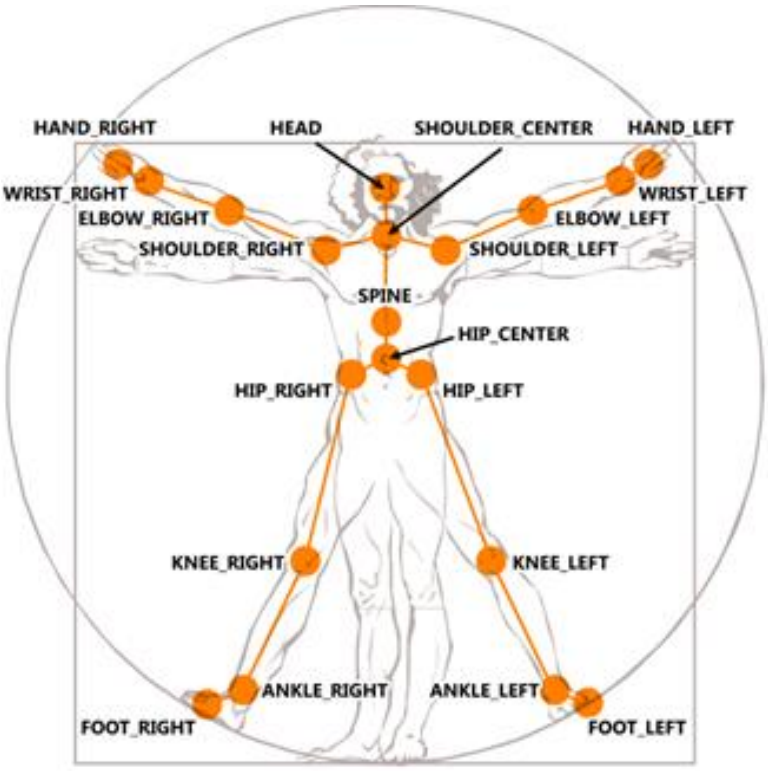

Figure 4.12 Kinect skeletal body part [9]

4.3 Human Robot Interaction

For the drone operation, the MS Kinect can receive the input as a form of gestures. Based on the body parts' coordinates retrieved in the previous section, skeletal and motion recognition algorithm is implemented using a kernel method and an artificial neural network (ANN). The rule-based algorithms such as nested if statements and for loops are not resilient enough to recognize a certain pattern, which differs every time. Due to the changing pattern, the rule-based algorithm does not output the robust results. When the output is not the desired result, the vehicle and the operator can be exposed to the serious damage.

Unlike the rule-based algorithm, ANN can process the pattern fast and classify the pattern with great resilient and thus the output has the high accuracy. Yet, the misclassification

as an output can result in the damage as well. To wrap the input gesture, a finite state machine is used. The overall algorithm is presented in figure 4.13.

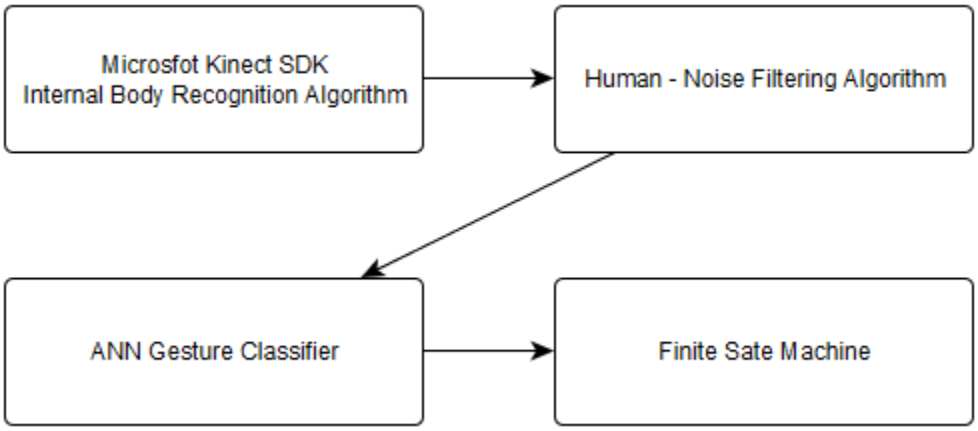

Figure 4.13 Kinect-based body gesture input algorithm

4.3.1 Human-Noise Skeletal Classification

The Kinect's original body part recognition algorithm is internally implemented in MSKSDK. Therefore, the MSKSDK merely outputs the skeletons recognized by the depth frame [47]. Since for the most of the time, Kinect is installed on a fixed object such as TV stand or a monitor, the probability of recognition of non-human object as a human is infrequent. However, Kinect is mounted on a drone in this project, and the flight causes vibrations, drifting, and rotation of the camera frame. Due to this reason, it is more likely for the internal depth frame-based body part recognition algorithm to output a set of body parts although it is not actually from a human in front of the camera. Without the human-noise classifier, the mere output of the skeletal frame can be misleading. Figure 4.14 shows a few sets of the skeletal frames before the classification. If the skeletal points due to the noise get into the gesture classifier, the untoward input from the noise skeleton can execute a command for the drone regardless of the operator's intention.

(a) Skeletal points on human body

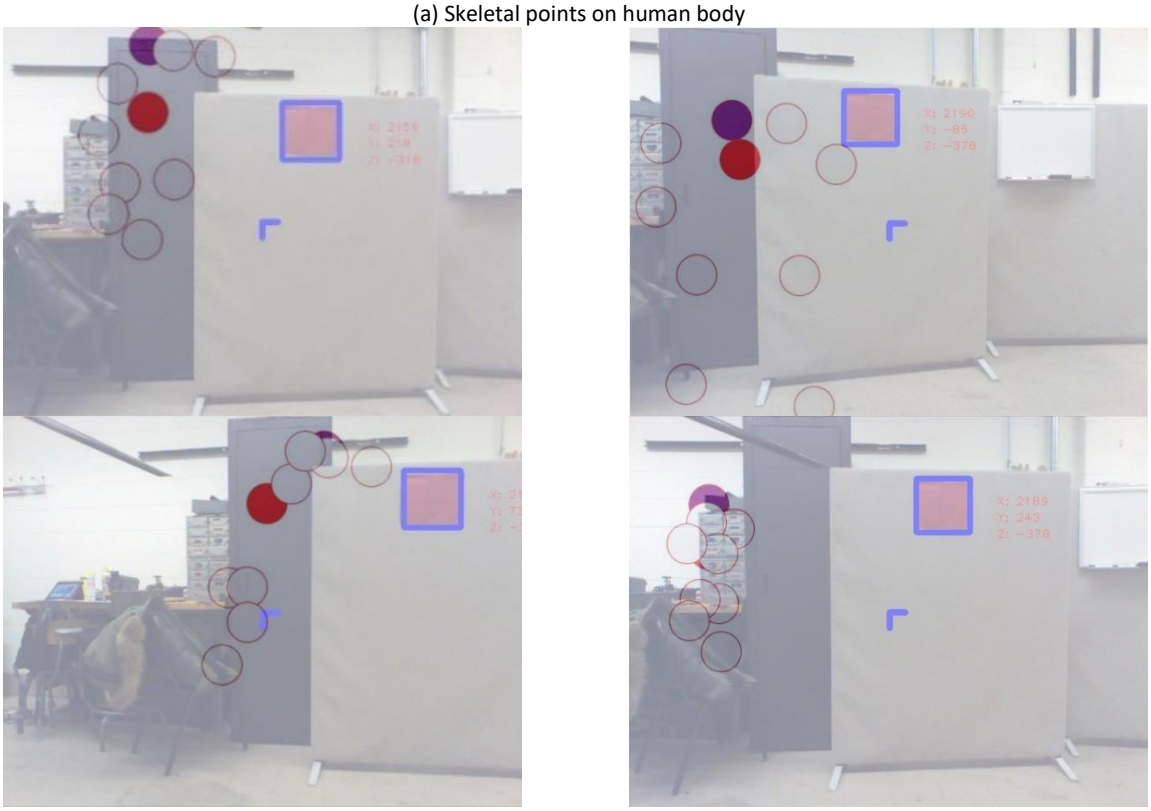

(b) Skeletal points due to noise

Figure 4.14 Unfiltered skeletal frames

For the data input for the classifier, left, center, and right shoulder and hip, head, and spine 3D coordinates are used. Since the raw relative coordinate of the 3D coordinates can vary as the position of the operator, all body part coordinates are convered to relative-to-center-shoulder. For instance, the center shoulder 3D coordinate changes as the operator's relative position to the camera changes while the other parts such as left hand 3D coordinate is always relative to the operator's centor shoulder location. Next, the collected body parts' 3D

coordiantes are put into a linear array. Since 7 body parts are used, the array size is 21. At the last column, or at 22nd column, the index of the corresponding class is attached. In this project, 1 is used for the coordinates from the actual human body parts while -1 is used for the coordinates due to the noise.

The human-noise classification algorithm employes kernel method to differentiate acutal human skeleton coordinates from those of noise [48,49]. In this project, Gaussian kernel is used.

$$\mathrm{K}(\mathrm{x_i}, \mathrm{x_j}) = e^{-\frac{\left\|x_i - x_j\right\|^2}{2\sigma^2}} \tag{4.4}$$

where x_i and x_j are the i^{th} and j^{th} data of the training set and σ is standard diviation of the Gaussian kernel. Then the optimization objective can be set as below representer theorem.

$$\mathrm{f}^* = arg\min_{f \in H} \frac{1}{n} \sum_{i=1}^{n} V(f(x_i), y_i) + \lambda \|f\| \tag{4.5}$$

where

- $f^*$is the optimal linear combination of the Gaussian kernel function that predicts the label,

  $f(x_i) = \alpha K(x, x_i)$ where α is $\mathrm{n} - \mathrm{dimensional\ vector}$
- $\mathrm{y_i}$ is the actual label,
- V is the loss function, $V = \frac{1}{2}(f(x_i) - y_i)^2$,
- n is for the number of data points in the training set,
- λ is a constant for regularization, and
- $||f||$ is a magnitude of the function values, it is used for the regularization.

The function f(x) will be used to predict the label of the skeletal coordinates of the body parts during the operation. The regularization term is added to penalize the functions that would over-fit the train data set. The equation 4.5 can be solved as shown in steps a) and b).

Step a) Solving the loss function

$$\frac{1}{n}\sum_{i=1}^{n} V(f(x_i), y_i) \;=\; \frac{1}{\mathrm{n}}\alpha^T K^2 \alpha - \frac{2}{n}\,\alpha^T K y + \frac{y^T y}{n} \tag{4.6}$$

Step b) Solving for the regularization term

$$\|f\| = \left\|\sum \alpha_i K\left(x_i\,, x_{input}\,\right)\right\|^2 = \alpha^{\mathrm{T}} K\,\alpha \tag{4.7}$$

Therefore, equation 4.5 can be reduced to

$$\mathrm{f}^* = arg\min_{\alpha} \frac{1}{\mathrm{n}}\alpha^T K^2 \alpha - \frac{2}{n}\,\alpha^T K y + \frac{y^T y}{n} \;+ \lambda\,\alpha^T K \alpha \tag{4.8}$$

To find the argument, α, that minimizes the function, the derivative is taken with respect to α.

$$\frac{2}{\mathrm{n}} K^2 \alpha - \frac{2}{n} K y + 2\lambda K \alpha = 0 \tag{4.9}$$

Finally, α can be found.

$$\alpha = (\mathrm{K} + \lambda \mathrm{nI})^{-1} y \tag{4.10}$$

To adjust λ and σ, cross validation is used [45, 48]. Figure 4.15 shows the results of the training and testing. The predicted values euqal to and larger than zero can be regarded as actual human skeletal coordinates while the values less than zero can be regarded as the skeletal coordinates from the noise.

The skeletal data due to noise can vary significantly as shown in figure 4.15b. That taking the boundary simple as 0 may not produce good prediction accuracy. Therefore, another constraint needs to be set to determine which can be regarded as the class with the index 1. From the figure 4.15 b, the labeled data's prediction result's distribution is shown in figure 4.15 c. For the specific data set shown here has the mean as 0.8313 with standard deviation of 0.2319. With confidence interval with 99%, the range can be deteremined as 0.9863 and 1.008 using equation 4.11 [50].

$$(\mu - 2.575 \times \sigma,\; \mu \;+ 2.575 \times \sigma\,) \tag{4.11}$$

where μ is the mean and σ is the standard deviation of the data shown in figure 4.14 c.

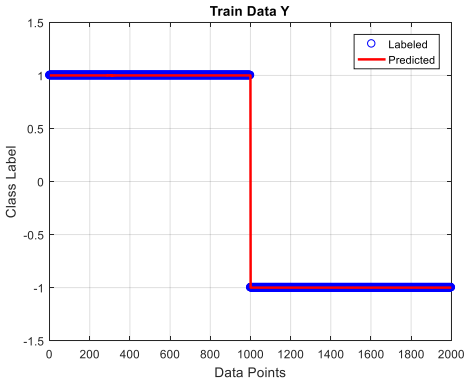

(a) Training data set result

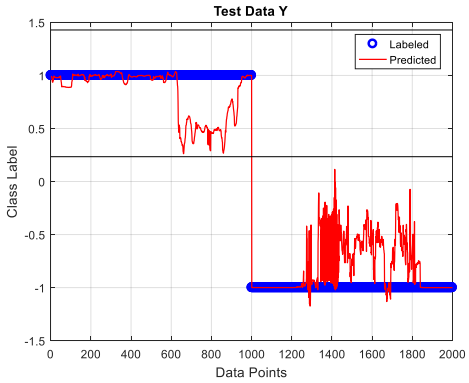

(b) Testing data set result

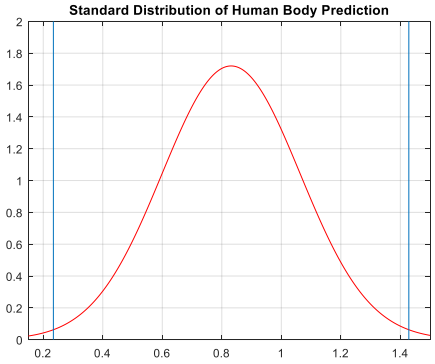

(c) Testing data set result

Figure 4.15 Traning and testing data set result

The algorithm is implemented on the onboard computer and the result is. (See figure 4.16.)

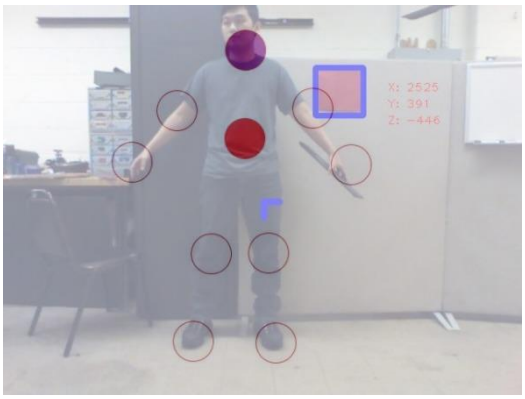

(a) Skeletal points of the human

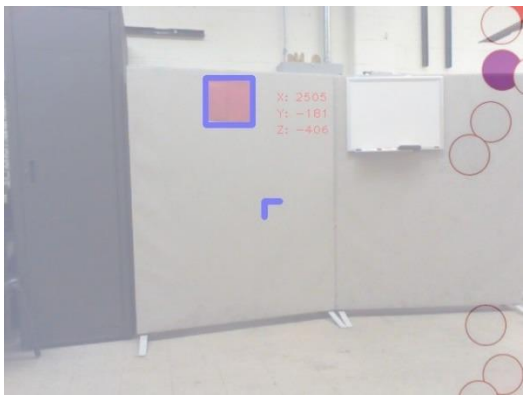

(b) Skeletal points due to noise

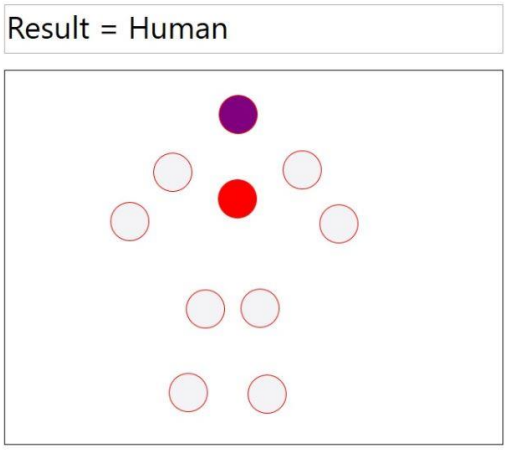

(c) Classification result based on human body parts

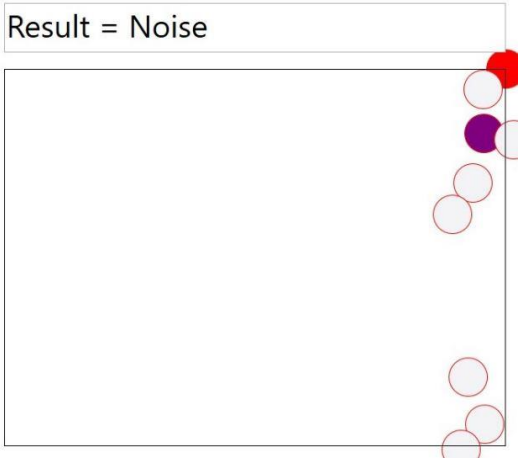

(d) Classification result based on the noise

Figure 4.16 Human-noise classification result

4.3.2 Gesture Recognition

A single hidden layered ANN algorithm is implemented for the gesture classification algorithm. As an input data, an operator's body parts coordinates are collected and labeled. The labels indicate the class type. In this project, take off, proceed, retreat, and landing gesture inputs are used.

4.3.2.1 Neural Network Design

The neural network implemented in this project has single hidden layer and one output layer as shown in figure 4.17. All neurons have bias connection. Hidden neurons use tangent

sigmoid function (equation 4.12) and output neurons have softmax function (equation 4.13) for their activation functions.

$$\text{tansig} = \frac{2}{1+e^{-2v}} - 1 \tag{4.12}$$

$$\text{softmax} = \frac{e^{v}}{\sum e^{v}} \tag{4.13}$$

where v is the dot product of input and weight vectors.

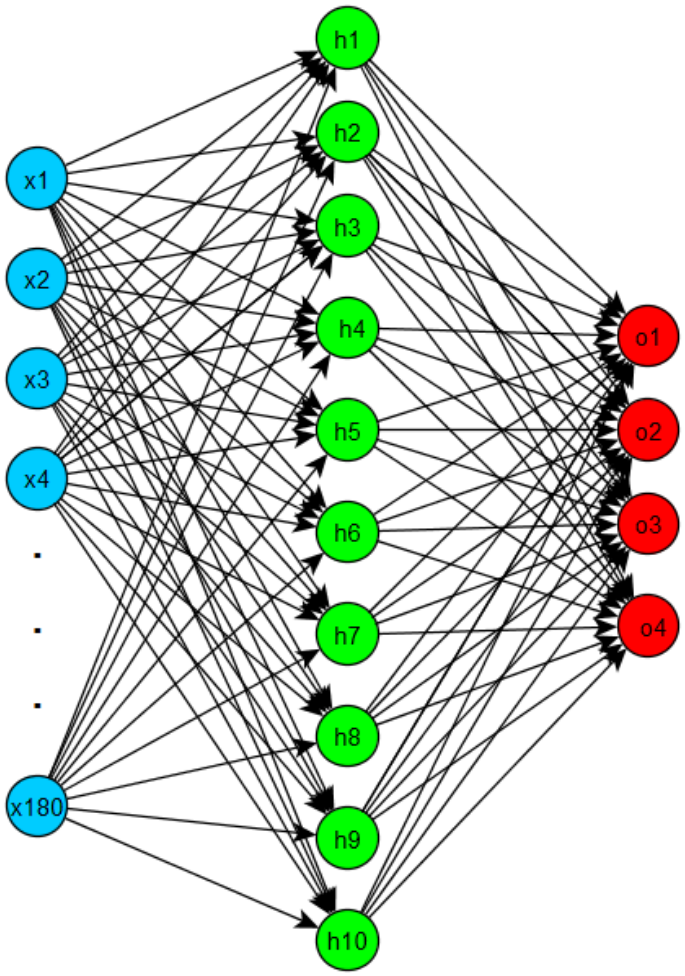

Figure 4.17 Artificial neural network, bias not shown

The forward propagation of ANN is expressed in equations 4.14 and 4.15.

$$the\ i^{th} neuron\ output\ in\ the\ hidden\ lyaer = \text{tansig}\left(\vec{x} \cdot \vec{w}_{h,i}\right) \tag{4.14}$$

$$the\ j^{th}\ neuron\ output\ in\ the\ output\ layer = softmax\left(\vec{h} \cdot \vec{w}_{j}\right) \tag{4.15}$$

where x is input vector in R^{180} and $\mathrm{w}_{\mathrm{h,i}}$ is the weight vector of i^{th} neuron in the hidden layer and $\vec{h}$ is the output vector of the hidden layer. In this project, bias is incorporated at every 0^{th} element of the input vectors for each layer.

4.3.2.2 Data Preprocessing

The input data is composed of two 3D vectors, left and right hand coordinates. During the flight, it can be confusing for the computer when the movement of the vehicle causes the relative movement of the body parts. To avoid this, the body part coordinate is subtracted by the mid-spine coordinate so that the other body parts coordinates are fixed relative to the mid-spine coordinate. Then these 3D vectors are collected for 1 second. Since the Kinect can offer the data at 30 Hz, total 30 data points are collected. Then the data set is linearly attached as an array with dimension of 180. Also, this array needs to be scaled from -1 to 1 to normalize the value. For the normalization mapminmax() function is used in Matlab and implemented in C# for the real-time computation. The function definition is shown in equation 4.16.

$$mapminmax(\overrightarrow{input}) = \frac{(1-(-1))\times(\overrightarrow{input}-\min(\overrightarrow{input}))}{\max(\overrightarrow{input})-\min(\overrightarrow{input})} + (-1) \quad (4.16)$$

where

- $\overrightarrow{input}$ is the 180-dimensional array.

In equation 4.16, 1 and -1 is used for the maximum and minimum values of the normalized array.

4.3.2.3 Training

The training process of the ANN is locating the minimum of the cost function. Although the algorithm can be stuck in a local minimum, in practice, resulting in global minimum is

frequent by randomizing the order of data [8]. The error and the error energy function at n^{th} epoch is defined as equation 4.17 and 4.18 [41].

$$\mathrm{e_k}(n) = d_k(n) - y_k(n) \tag{4.17}$$

$$\mathrm{E_k}(n) = \frac{1}{2} e_k^2(n) \tag{4.18}$$

where

- $\mathrm{d_k}$ is the label or desired output of the k^{th} input vector, and
- $\mathrm{y_k}$ is the output of the forward propagation of the k^{th} input vector.

By summing the error energy functions by all data point, the total cost function is defined and gradient descent rule is applied [45].

$$E(n) = \frac{1}{2}\sum_k [d_k(n) - \ y_k(n)]^2 = \frac{1}{2}\sum_k \left[d_k(n) - \psi\left(\sum_j w_{kj} y_j\right)\right]^2 \tag{4.19}$$

where

- ψ is the activation function of a neuron, and
- j is j^{th} neuron from the previous layer.

To find the minimum error energy function, the partial derivative can be taken with respect to weight.

$$\frac{\partial \mathrm{E}}{\partial \mathrm{w_{kj}}} = \ -\mathrm{e_k}\psi'(v_k) y_j \tag{4.20}$$

Therefore, the weight vectors of output layer at $(n+1)^{th}$ iteration is

$$w_{kj}(n+1) = w_{kj}(n) + \eta e_k(n)\psi'(v_k) y_j(n) \tag{4.21}$$

Similarly, weight update for the hidden layer can be calculated.

$$w_{ji}(n+1) = w_{ji}(n) + \eta\psi'\left(v_j(n)\right)\left[\sum_k w_{kj}(n)\, e_k(n)\psi'(v_k)\right] x_i(n) \tag{4.22}$$

where

- i indicates i^{th} input.

In Matlab, Pattern Net in the Neural Network toolbox is used to expedite the back propagation process. Then, the weight vectors of the Matlab is imported to the Kinect software in C# so that the real-time body coordinates can be fed into the forward propagation algorithm shown the previous chapter. For the training, 2000 data points are collected for each class. Therefore, 8000 data points are collected in total for the four different classes of the body gesture: take-off, landing, proceed, and retreat with the corresponding labels of 1, 2, 3, and 4 respectively. Figure 4.18 shows the gesture labels.

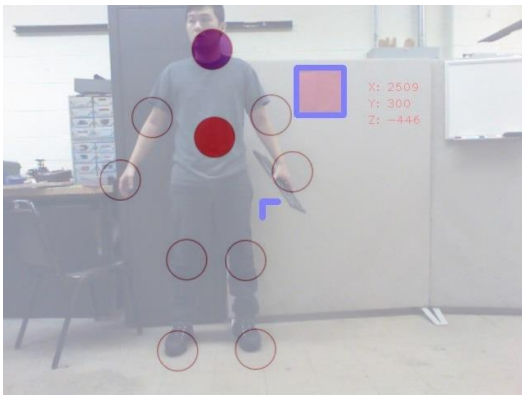

(a) Class1: idle gesture

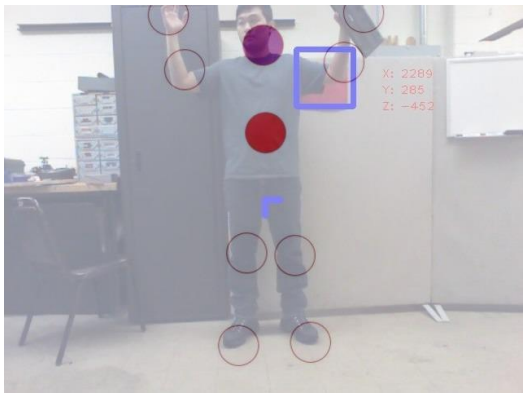

(b) Class2: take off / landing gesture

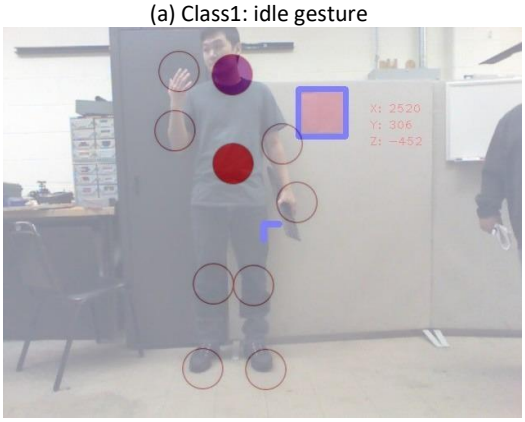

(c) Class3: proceed gesture

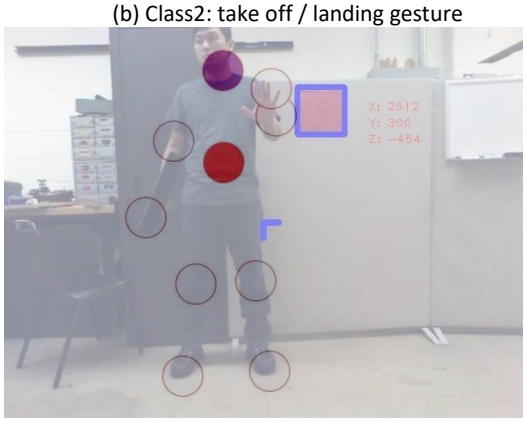

(d) Class4: retreat gesture

Figure 4.18 Gestures of four classes

The Matlab's toolbox shows the training process in Cross-Entropy, figure 4.19.

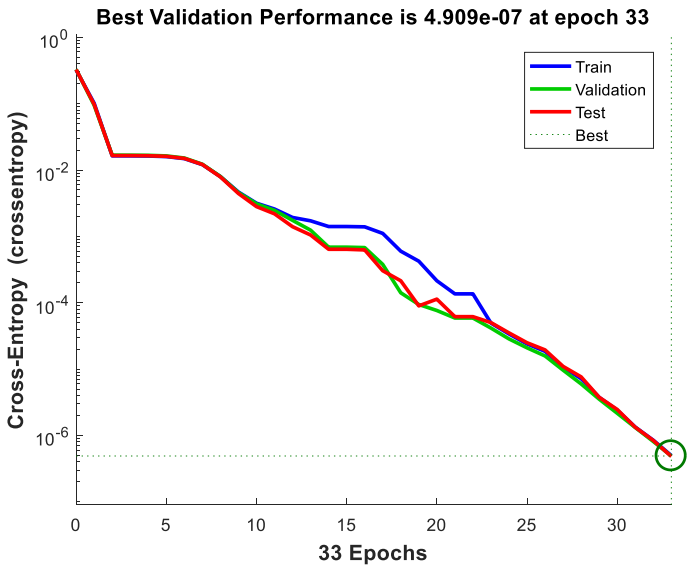

Figure 4.19 Training performance

Since the body gestures used in the project is only 4 types with distinctive space and with a steady camera, the accuracy can be 100 percent. Figure 4.20 shows the classification result.

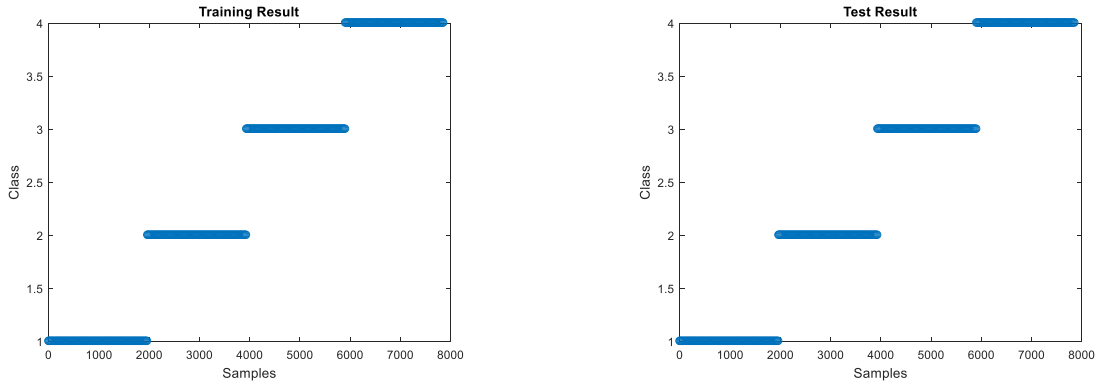

Figure 4.20 Classification result of the training (left) and testing (right) sets

4.3.3 Finite State Machine

A finite state machine (FSM) is used to suppress misclassification result during the operation. The misclassification is primarily due to the noise generated by the moving frame.

Also, when a body part is not detected or outside of the frame, Kinect's built-in body part recognition algorithm's estimation accuracy can drastically deteriorate, which results in outputting the 3D coordinates with low accuracy.

The FSM has three states in this project: ground, preflight, and tracking as shown in figure 4.21. FSM can receive any input. Yet, it reacts to specific sets of input. Table 4.1 lists the states, inputs, and outputs of the FSM. Since FSM only reacts to a certain input types, it is safe to interface the INS because wrong input (ANN misclassification) can be directly sent to the INS, which does not have the algorithm for context-depending decision rules, and the wrong input can cause malfunctioning during the operation. Such unexpected operation can result in structural damage.

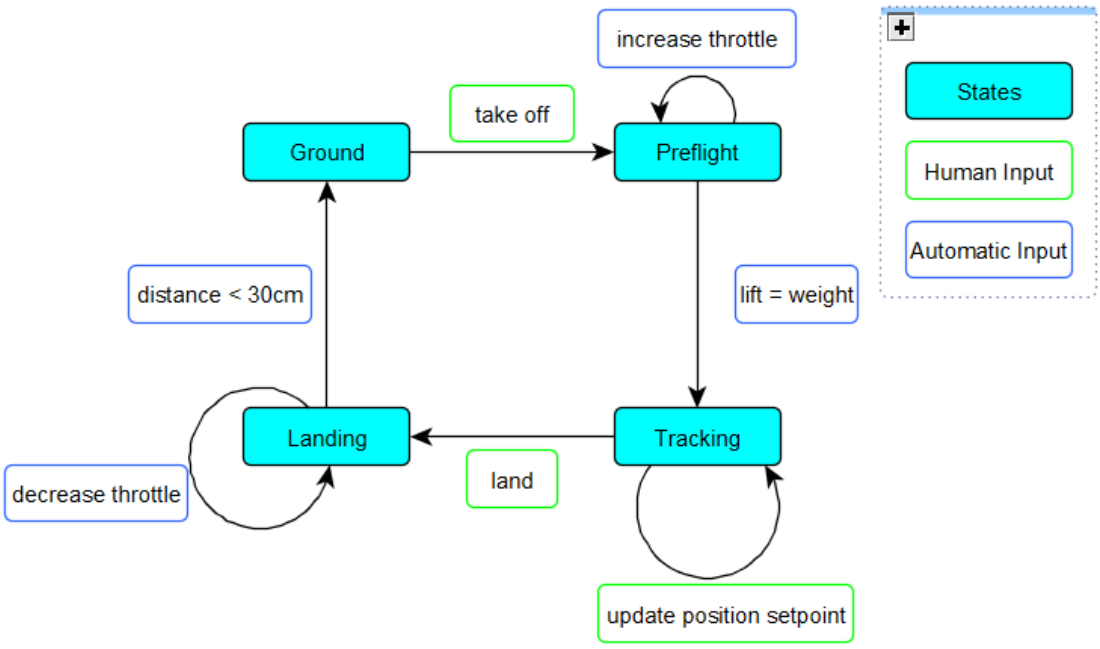

Figure 4.21 Finite state machine for 4 different flight modes

Table 4.1 State Transition Table

Current State	Possible Input	Output	Next State
Ground	none	none	Ground
	take off	turn on attitude PID Controller	Preflight
	landing	none	Ground
	proceed	none	Ground
	retreat	none	Ground
	time elapse	none	Ground
Preflight	none	increase throttle	Preflight
	take off	none	Preflight
	landing	none	Preflight
	proceed	none	Preflight
	retreat	none	Preflight
	time elapse	turn on position PID controller	Tracking
Tracking	none	none	Tracking
	take off	none	Tracking
	landing	lower height setpoint	Tracking
	proceed	decrease distance setpoint	Tracking
	retreat	increase distance setpoint	Tracking
	time elapse	none	Tracking
Landing	Distance <= 30 ?	turn off PID controllers	Ground
	distance > 30 ?	decrease throttle	Landing
	take off	none	Landing
	landing	none	Landing
	proceed	none	Landing
	retreat	none	Landing
	time elapse	none	Landing

In figure 4.21, the human input is the output of the ANN classification result. ANN can output FSM input such as “take off”, “proceed”, “retreat”, and “land”. The automatic input is generated by the specific state that is not accessible by an operator during the mission. During the inaccessible states such as “Preflight” and “Landing”, the FMC iterates an open and closed loops respectively. During the state of “Preflight”, FMC sends messages to INS to gradually increase the throttle to a pre-determined pulse width modulation (PWM) so that the lift generated by the propellers is slightly lower than the weight. Similarly, during the state of “Landing”, FMC

sends messages to gradually decrease the throttle based on the ultrasonic distance sensor reading. When the distance sensor reading is less than 30cm, the state of “Landing” switches to the state of “Ground”.

Chapter 5. Inertial Navigation System

5.1 Introduction

This chapter discusses how the IMU is integrated with other MCUs (See figure 5.1). Since single Parallax Propeller module has 8 cogs, to parallel-process several routines during the mission, inertial navigation system (INS) in this project needs four MCU boards. The first module is used for IMU, discussed in chapter 3. Other important aspects of the navigation system are controller and data sharing with each other. In chapter 5.2 and 5.3, the controller and the data sharing algorithm is presented. Communications with the ground control station and flight management computer is discussed in chapter 6.

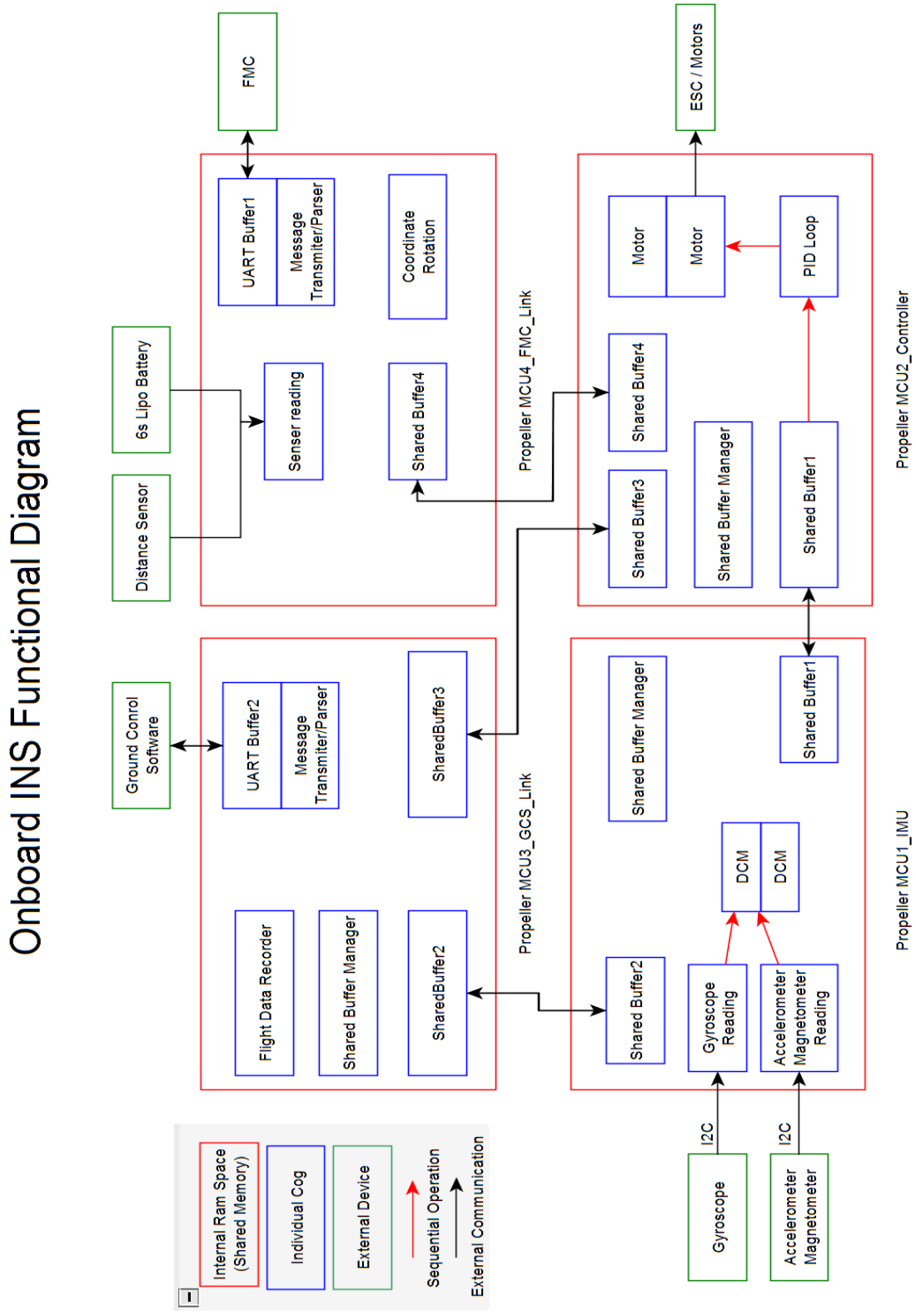

Figure 5.1 Parallax Propeller microcontroller-based inertial navigation system

5.2 PID Controller / ESC Driver Implementation

5.2.1 ESC Driver

Pulse width modulation (PWM) is a digital signal that contains the information regarding duty cycle. For a motor control, duty cycle can be viewed as a variable controlling the RPM of the motor. As shown in figure 5.2, 10 or 50 percent of duty cycle outputs the corresponding percentage of the maximum RPM of the motor.

Table 5.1 Pulse width modulation generation for a motor

```
1   initialize pin                          // a pin to output the signal
2   initialize highTime                     // time for the high signal. ex) 0.5 for figure 5.2 (b)
3   repeat
4       set high signal for a pin
5       maintain the high signal for highTime
6       set low signal for a pin
7       wait for ( period - highTime )      // keeping the exact period
```

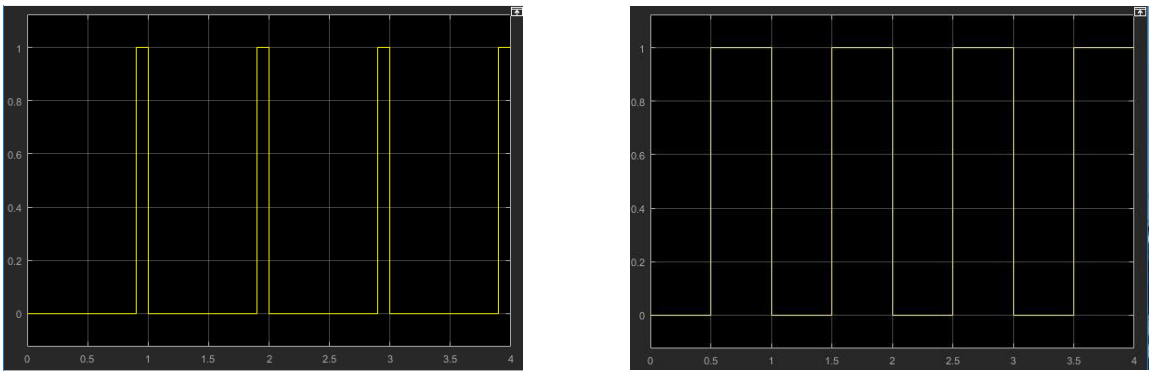

(a) 10 percent duty cycle **(b) 50 percent duty cycle**

Figure 5.2 Pulse width modulation, period = 1 second

As presented in chapter2, the electric speed controller (ESC) used in this project can receive the signal with frequency between 30 to 450 Hz, or with the periods of 0.0022 to 0.0333 seconds. For the best efficiency of the INS, the input frequency is set as 150Hz because the maximum update rate of the IMU is 150Hz. Also, for the single motor, the maximum time for the high signal is approximately 0.002 second, which is slightly shorter than the minimum period. To

operate the 6 ESCs at 0 to 100 percentage of the capacity, using one cog of the MCU cannot be sufficient. As shown in Table5.2 line 9, the possible total time elapse can be $0.002 \times 6 = 0.012$ second, which is longer than 0.006 second, the period for 150 Hz. To maintain 150Hz input, two cogs of the MCU have to be exploited. Each cog operates 3 ESCs. Therefore, the array size in Table 5.2 line 1 and 2 is 3 rather than 6 while the same code is used for another cog that controls the rest of the three motors.

Table 5.2 Pulse width modulation generation

```
1   initialize pin[6]              // initialization of microcontroller's pins, 6 pins for a hexacopter
2   initialize highTime[6]         // initialization of the time elapse of the high signal for 6 ESCs
3   repeat
3       initialize totalElapse = 0     // initialization of the variable to store the total highTime
4       for each i
5           set high signal for pin[i]
6           maintain the high signal for highTime[i]
7           set low signal for pin[i]
8           totalElapse += highTime[i]
9       wait for ( period - totalElapse )     // keeping the exact period
```

To update the RPM, the variable "highTime[i]" needs to be updated. The amount of the change is calculated by an attitude controller.

5.2.2 Attitude PID Controller

For the stability of the attitude and position of the vehicle, proportional integral derivative (PID) controllers are implemented [52, 54].

$$u(t) = K_p e(t) + K_i \int e(t)dt + K_d \frac{de(t)}{dt} \quad (5.1)$$

where, K_p is proportional gain, K_i is integral gain, K_d is derivative gain, e(t) is error signal, $u(t)$ is the output of the controller, and the function argument t is time. The block diagram of PID controller and a reduced block is shown in figure 5.3. PID controller receives error signal. The error is the difference between the reference and sensor signals.

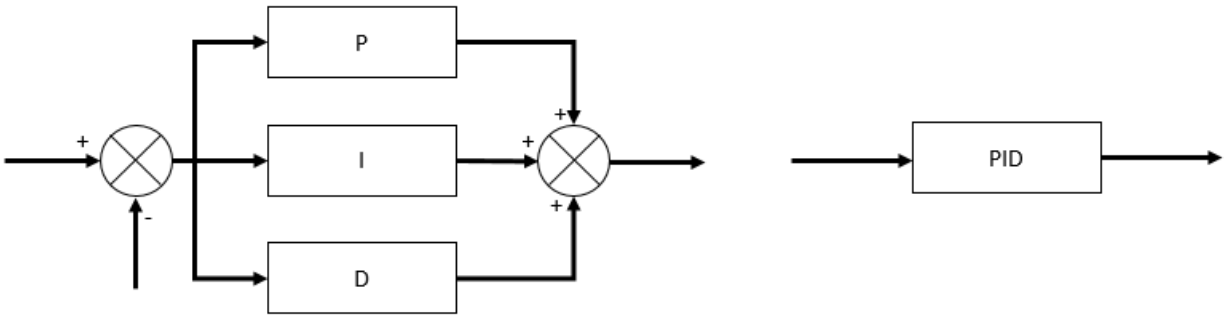

Figure 5.3 PID Blocks (left) and reduced block (right)

The proportional block outputs a signal to compensate the error. The magnitude of the proportional signal is determined by the proportional gain, $\mathrm{K_p}$. To reduce the amount of overshoot, the derivative block outputs a signal based on the derivative of the error signal with respect to time. Similarly, the amount of the derivative signal is determined by the derivative gain, $\mathrm{K_d}$. Lastly, to compensate the steady state error, the integral block outputs the integration of the error signal. The amount is determined by the integral gain, $\mathrm{K_i}$. Lastly, the total output is the summation of the outputs from the three blocks.

For the attitude controller, a digital PID controller is implemented. The sensor reading is based on the IMU. The digital PID controller algorithm is shown in Table 5.3.

Table 5.3 PID controller algorithm

1	repeat
2	for each Euler angle
3	error = reference – current angle
4	proportional = $\mathrm{K_p} \times$ error
5	derivative = $\mathrm{K_d} \times$ (error – prev_error) / Δt
6	integral += $\mathrm{K_i} \times$ error
7	output = proportional – derivative + integral
8	previous error = error

The attitude PID controller needs the inputs as three Euler angles at each iteration. For pitch control, motor number 1, 2, 4, and 5 are updated. For Roll control, motor number 1, 2, 3, 4, 5, and 6 are updated. For yaw control, motor number 1, 2, 3, and 5 are updated (See figure

2.1). Figure 5.4 shows the block diagram of the attitude PID controller. The error signals are calculated as discussed previously. In this case, the error is the difference between the reference Euler angles from the position PID controller and the current Euler angles. Especially, the yaw PID controller error calculation needs a preprocessing step. Since the Euler angle output range for the yaw varies from -180 to 180, the proportional term can overshoot significantly although -180 and 180 both indicate the same direction: South. The yaw controller overshoots when the magnitude of the error is greater than 180 degrees. For instance, when the set point of the heading is -179 degree and the current heading is 179, the error calculation shown in table 5.3 ends up in -358, which will take the longer angular path of 358 degrees rather than 2 degrees to the opposite direction. To prevent the overshoot, the error larger than 180 degrees can be subtracted by 360 whereas the error smaller than -180 degrees can be added by 360.

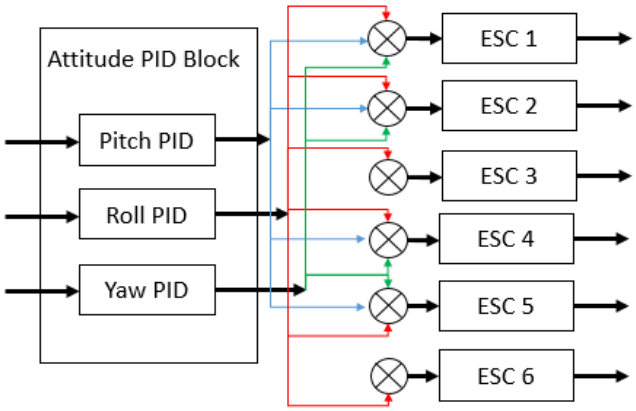

Figure 5.4 Attitude PID controller

Using Matlab built-in function system identification, the transfer function can be estimated based on the step input and output data collected from the vehicle. Figures 5.5 - 5.7 show the performance analysis of the pitch PID controller.

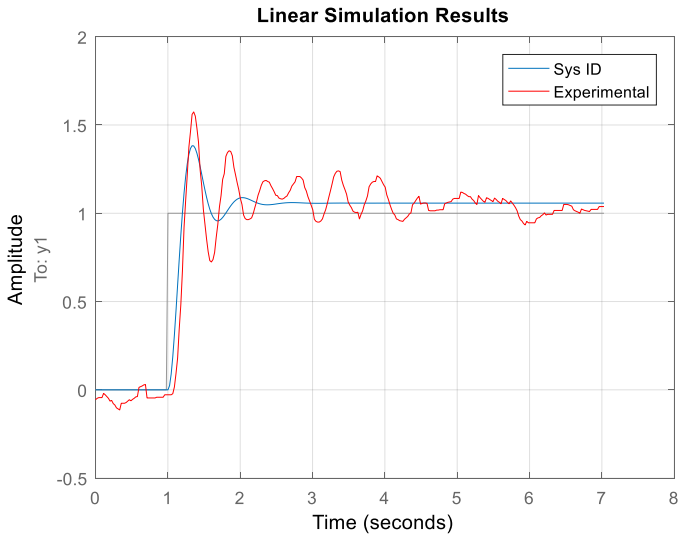

Figure 5.5 Pitch PID controller simulation and experiment output

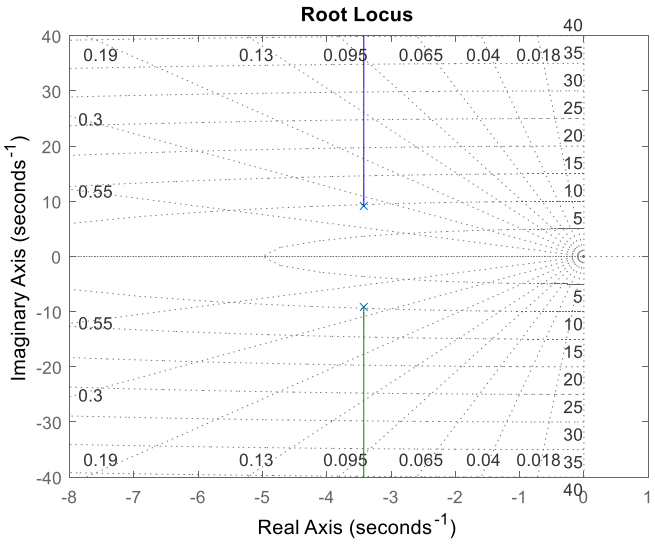

Figure 5.6 Root locus for the pitch PID controller and plant

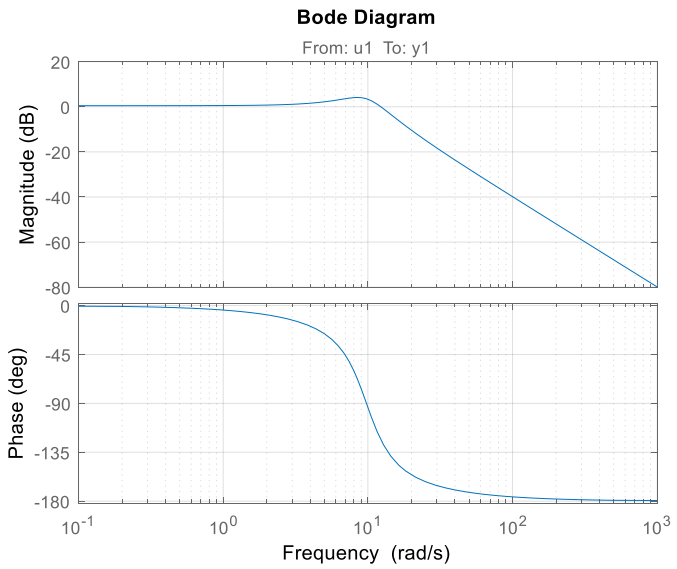

Figure 5.7 Bode plot for the pitch PID controller and plant

The pitch controller is assumed to be a second order system. The estimated transfer function is

$$\text{pitch(s)} = \frac{101}{s^2+6.848s+95.52} \tag{5.2}$$

As shown in figures 5.6 and 5.7, the system meets stability criterion [52, 54]. Also, the performance analysis is listed as below.

Table 5.4 Pitch PID controller performance

Rise Time	0.166 (s)
Settling Time	3.1918 (s)
Overshoot	34.7563 (%)
Peak	1.4389
Peak Time	0.3501 (s)
Gain Margin	∞ (dB)
Phase Margin	56.51 (deg)

Similarly, the roll PID controller is analyzed. Figures 5.8 - 5.10 show the performance analysis of the roll PID controller.

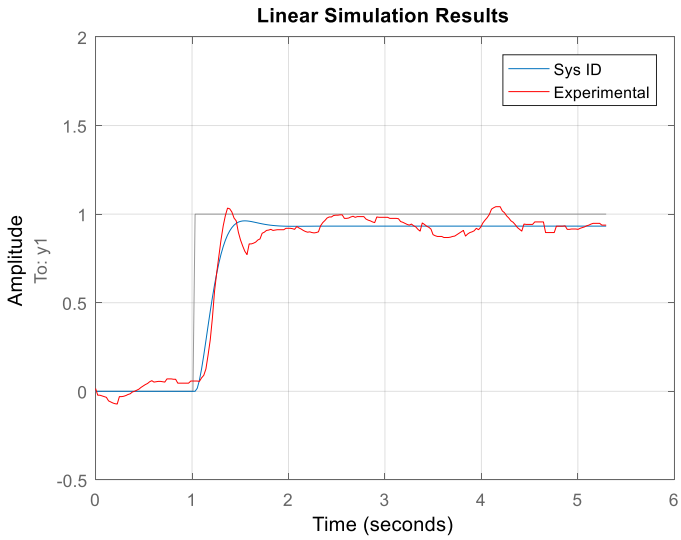

Figure 5.8 Roll PID controller simulation and experiment output

The roll controller is assumed to be second order system. The estimated transfer function is

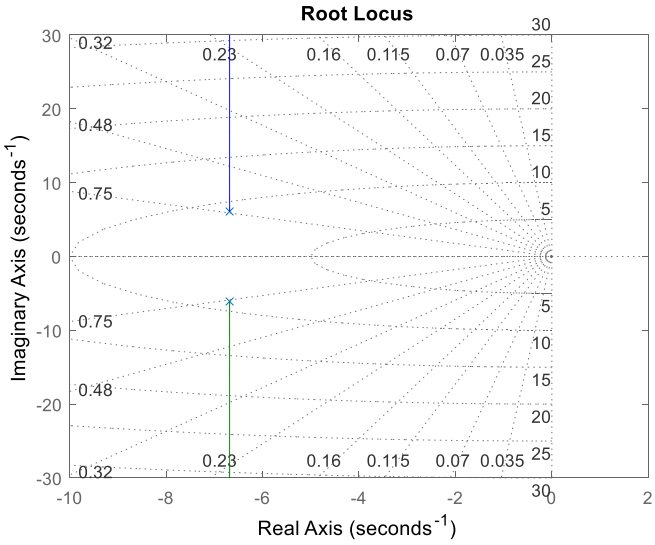

Figure 5.9 Root locus for the roll PID controller and plant

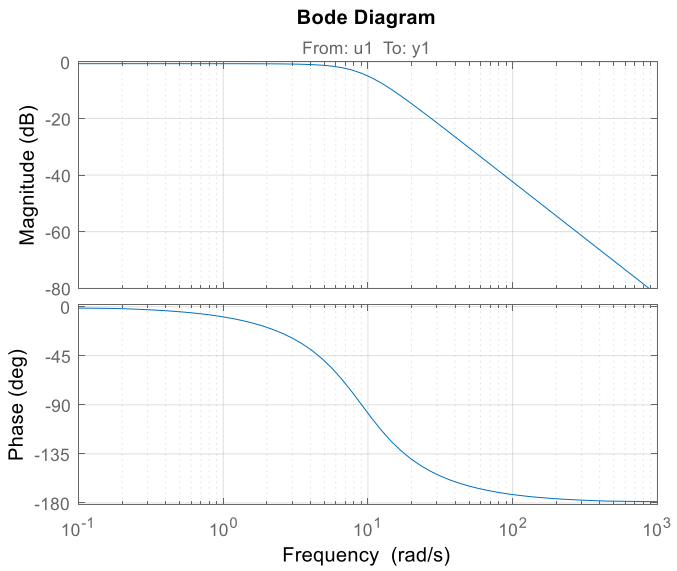

Figure 5.10 Bode plot for the roll PID controller and plant

The performance of the roll PID controller is listed as the table below.

$$\text{roll(s)} = \frac{76.26}{s^2+13.36s+81.8} \tag{5.3}$$

Table 5.5 Roll PID controller performance

Rise Time	0.3017 (s)
Settling Time	0.6444 (s)
Overshoot	3.1944 (%)
Peak	0.9621
Peak Time	0.5169 (s)
Gain Margin	∞ (dB)
Phase Margin	∞ (deg)

Finally, the yaw PID controller is shown in figures 5.11 - 5.13.

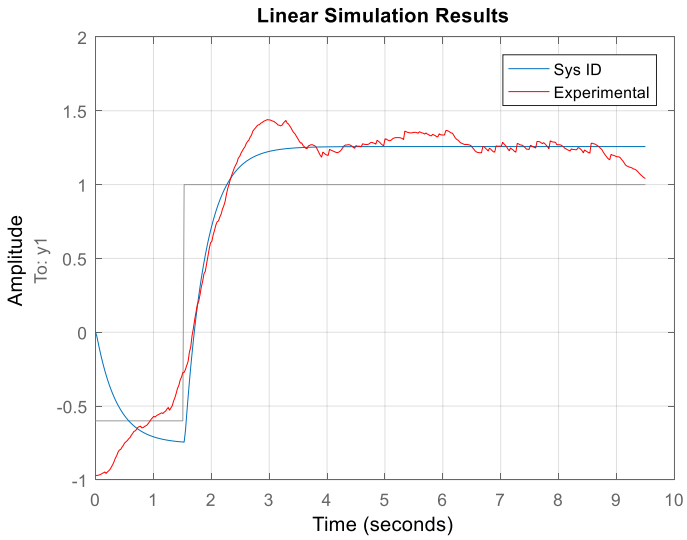

Figure 5.11 Yaw PID controller simulation and experiment output

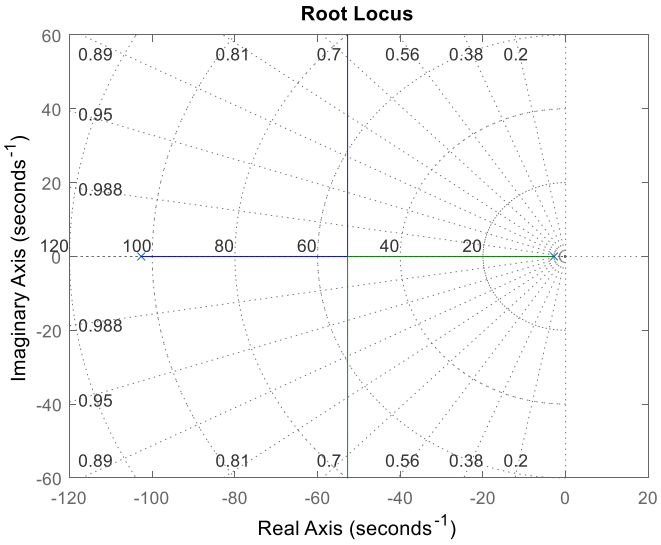

Figure 5.12 Bode plot for the yaw PID controller and plant

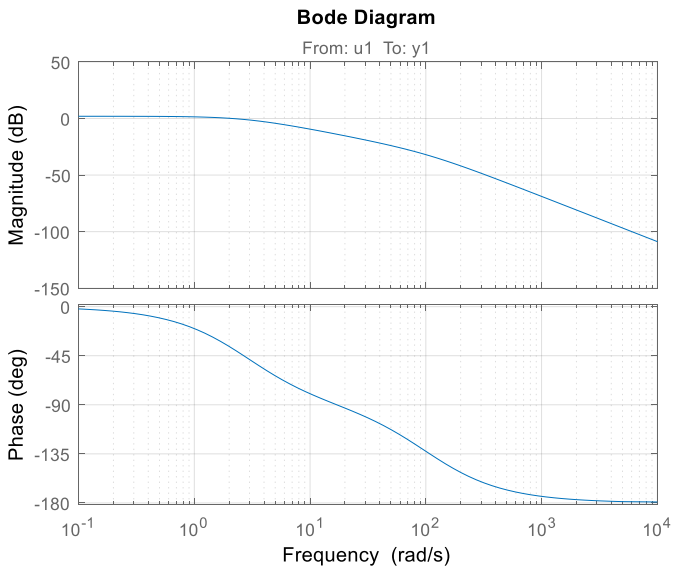

Figure 5.13 Bode plot for the yaw PID controller and plant

$$\text{yaw(s)} = \frac{363.4}{s^2+0.5.56s+288.9} \tag{5.4}$$

Table 5.6 Yaw PID controller performance

Rise Time	1.0471 (s)
Settling Time	1.3999 (s)
Overshoot	0 (%)
Peak	1.2568
Peak Time	2.6016 (s)
Gain Margin	∞ (dB)
Phase Margin	141.4922 (deg)

5.2.3 Position PID Controller

The position PID controller has the same essence as the attitude controller as depicted in figure 5.14. For longitudinal and translational movements, the reference angle for the pitch and roll is updated by the position PID controller. The height or z-axis controller is based on either vision or ultrasonic distance sensor and updates throttle of the collective motors. Vision

sensor is primarily used to maintain the vertical distance to the target while ultrasonic is used for landing and taking-off routines.

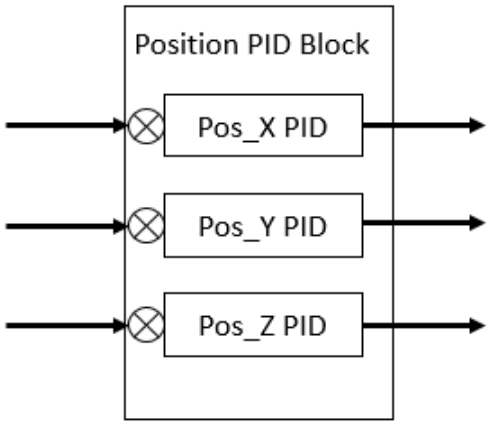

Figure 5.14 Attitude PID controller

Figure 5.15 shows the overall block diagram of the PID controller cascade. The inner loop is the attitude controller and the outer loop is the position controller. The vision sensor is input is from the FMC. The gains of the both controllers are empirically determined.

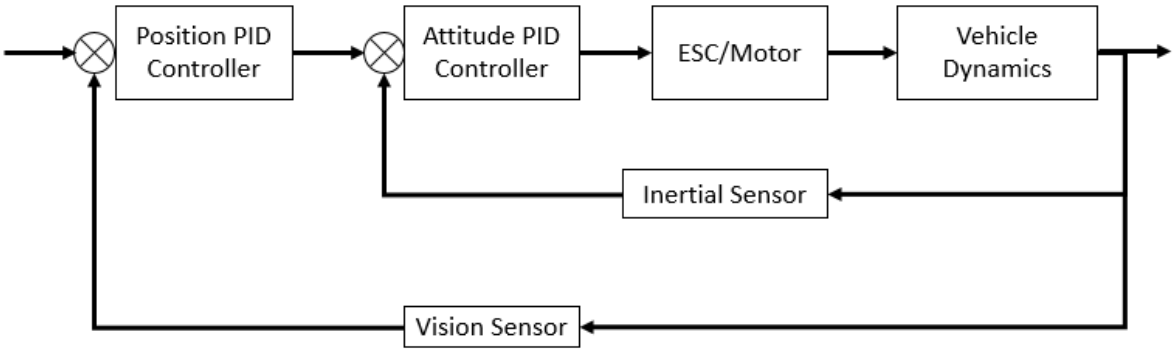

Figure 5.15 Cascade of PID controller block diagram

Figures 5.16 – 5.24 show the performances of x, y, z axes of the position PID controller. Also, the tables 5.7 – 5.9 show the performance details of the controller.

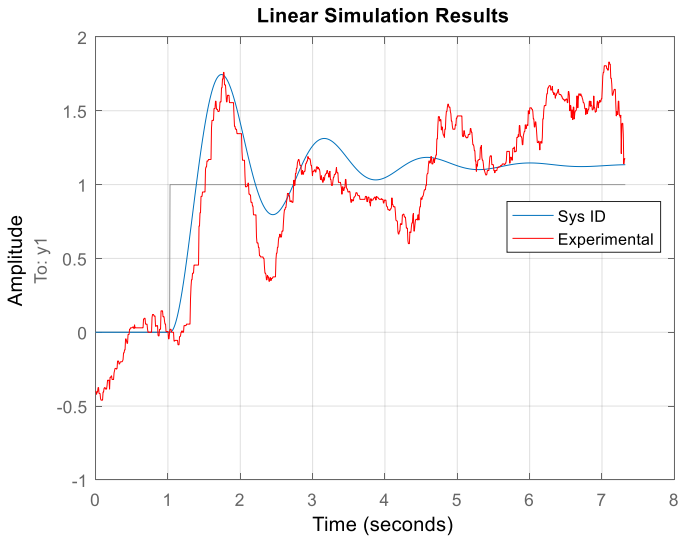

Figure 5.16 X-directional position PID controller simulation and experimental output

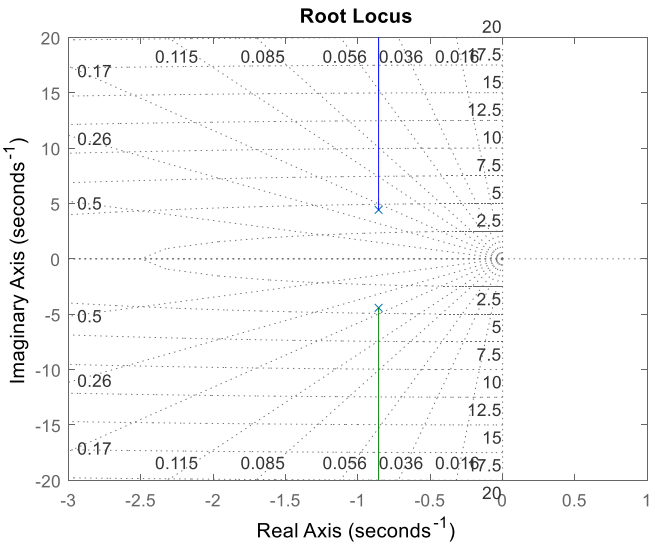

Figure 5.17 Root locus for X-direction position PID controller

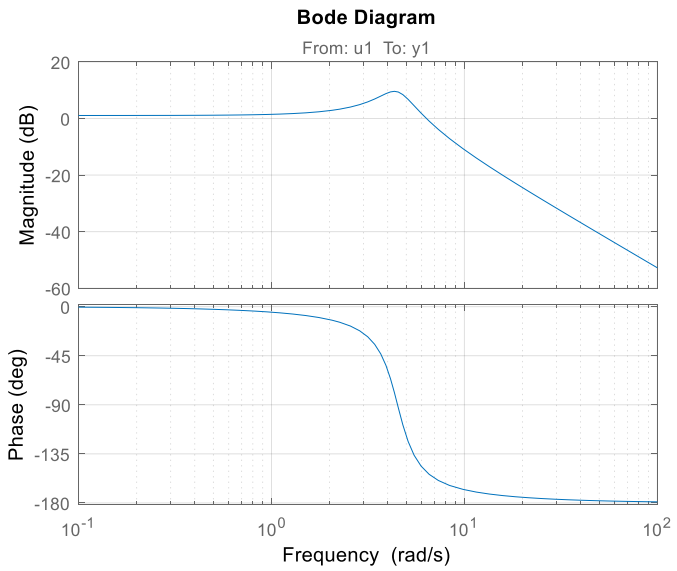

Figure 5.18 Bode plot for X-directional position PID controller

$$\text{Position\_X(s)} = \frac{22.92}{s^2+1.714s+20.27} \tag{5.5}$$

Table 5.7 X-directional PID controller performance

Rise Time	0.3152 (s)
Settling Time	4.4226 (s)
Overshoot	54.2921 (%)
Peak	1.7445
Peak Time	0.6984 (s)
Gain Margin	∞ (dB)
Phase Margin	28.3985 (deg)

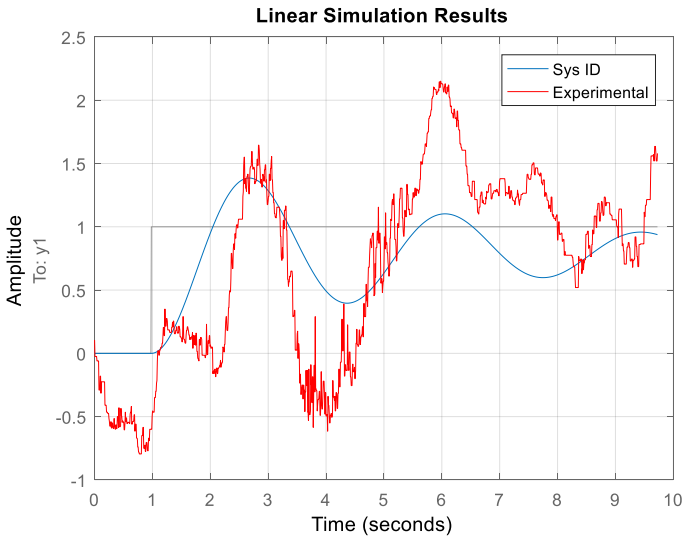

Figure 5.19 Y-directional position PID controller simulation and experimental output

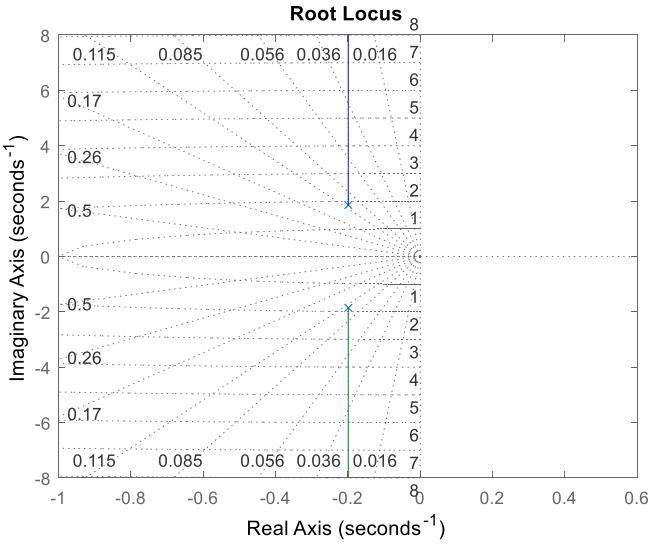

Figure 5.20 Root locus for Y-direction position PID controller

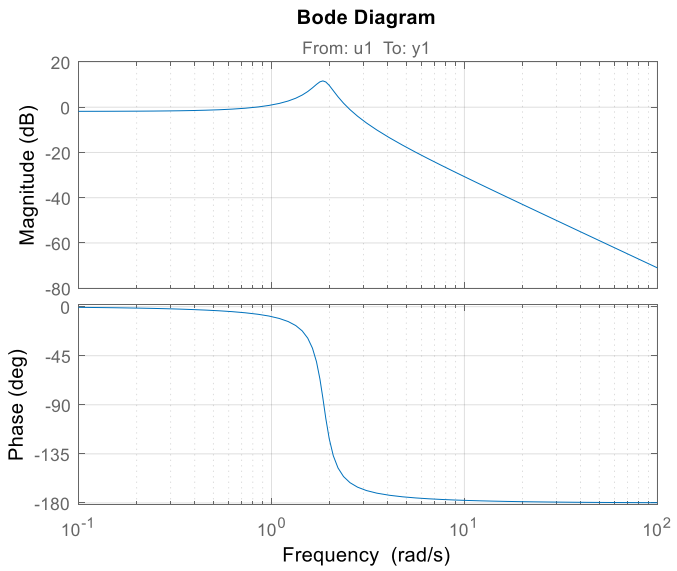

Figure 5.21 Bode plot for Y-directional position PID controller

$$\text{Position\_Y(s)} = \frac{2.819}{s^2+0.3983s+3.488} \tag{5.6}$$

Table 5.8 Y-directional PID controller performance

Rise Time	0.7015 (s)
Settling Time	18.9399 (s)
Overshoot	71.3857 (%)
Peak	1.3850
Peak Time	1.6820 (s)
Gain Margin	∞ (dB)
Phase Margin	20.4712 (deg)

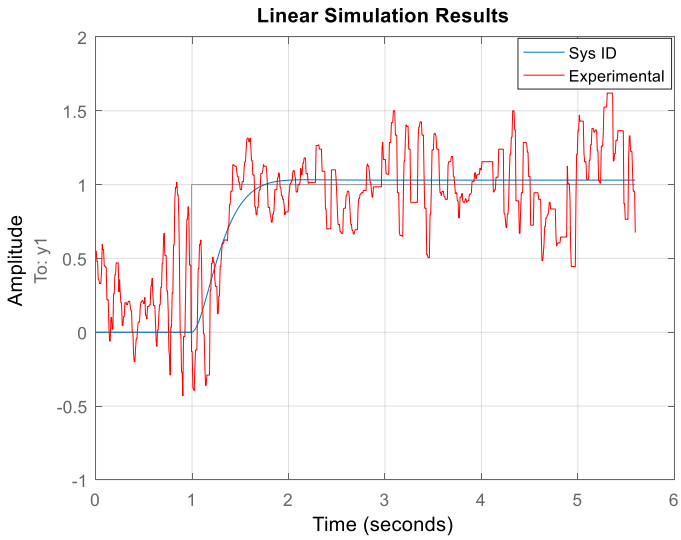

Figure 5.22 Z-directional position PID controller simulation and experimental output

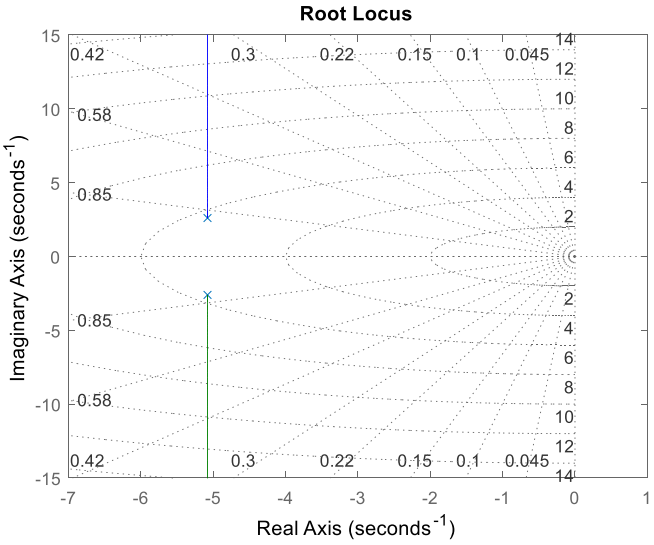

Figure 5.23 Root locus for Z-direction position PID controller

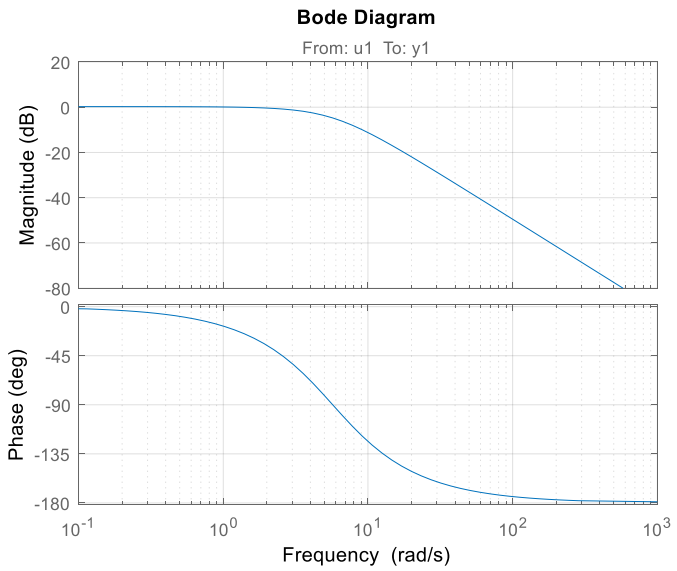

Figure 5.24 Bode plot for Z-directional position PID controller

$$\text{Position\_Z(s)} = \frac{33.57}{s^2+10.16s+32.58} \tag{5.7}$$

Table 5.9 Z-directional PID controller performance

Rise Time	0.6298 (s)
Settling Time	0.8045 (s)
Overshoot	0.2178 (%)
Peak	1.0327
Peak Time	1.2058 (s)
Gain Margin	∞ (dB)
Phase Margin	157.0979 (deg)

Finally, the position maintenance result of the drone for the fixed set point for each axis is shown in figure 5.25.

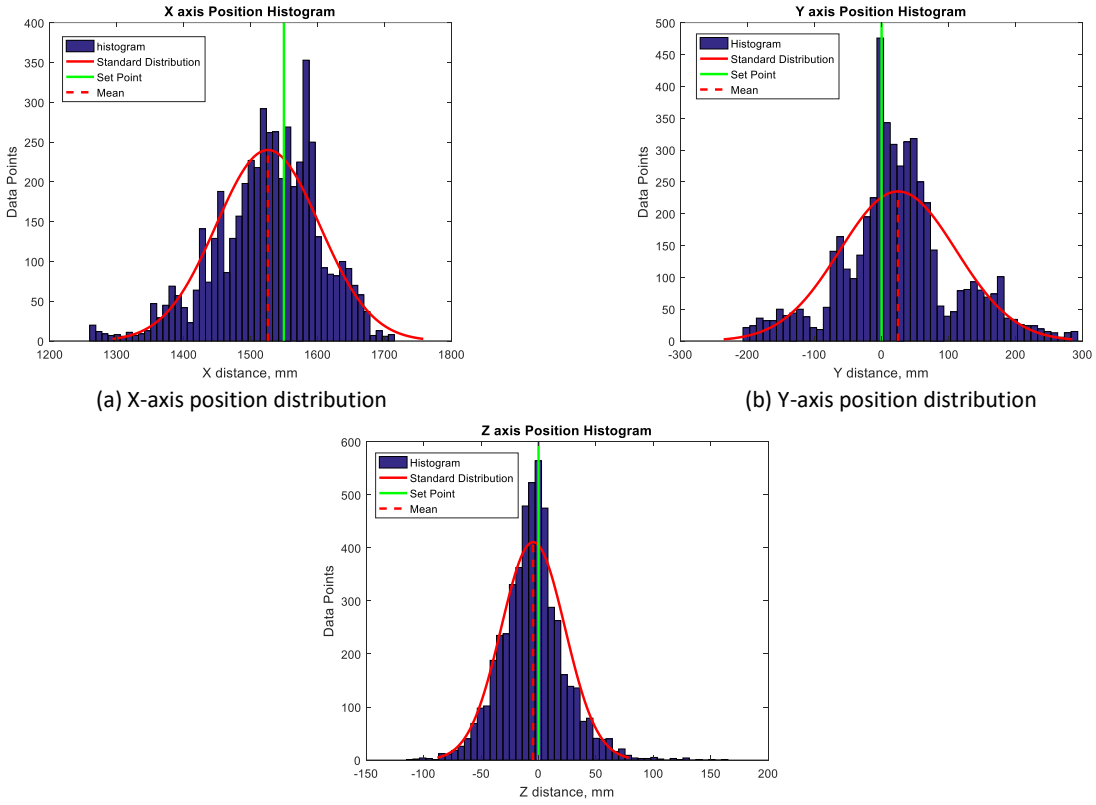

(a) X-axis position distribution

(b) Y-axis position distribution

(c) Z-axis position distribution

Figure 5.25 Histogram of position maintenance

5.3 System Integration

5.3.1 Microcontroller Integration

Since the INS is composed of four individual Parallax Propeller MCU boards, the data have to be shared. Figure 5.5 shows that the inertial sensor input is from the IMU and the PID controller algorithms are implemented on the second chip. Using the chip communication library offered by Dr. McCrink, the two chips can share the memory space as shown in figure 5.26.

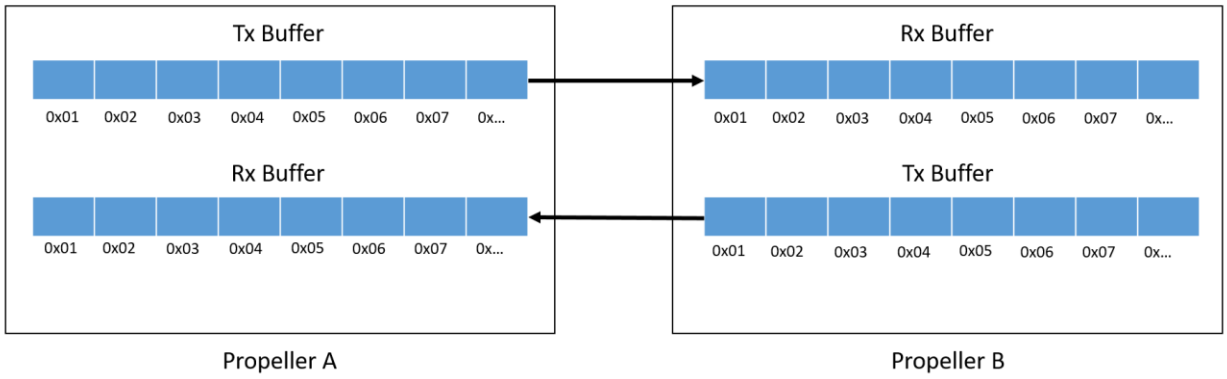

Figure 5.26 Propeller microcontroller communication buffers

This communication link is used for the data sharing among the MCU boards. In figure 5.1, the black arrows between shared memory block indicate this communication link. To manage these sets of Tx and Rx buffers, an algorithm to manage the information in the buffer is needed to prevent an element of array can be directly used for the drone operation. For instance, an element of the Rx buffer in Propeller B can be a message such as the output of the attitude PID controller to increase the angular speed of a motor. Once the motor speed is increased, the motor speed should stop increasing. Yet, the piece of the information still remains in the Rx buffer and this does not limit the increment. To address this issue, which is similar to a producer-consumer problem, one more piece of information is attached to indicate availability of the information [53]. For instance, when Propeller A receives the information to increase motor number 2 from GCS, it post the information in a two contiguous memory. For instance, 0x01 and 0x02 of Tx buffer of a producer, Propeller A. At 0x01, the motor number, 2, is posted, and the amount of increment is posed at 0x02. Once Propeller B, a consumer, receives the corresponding data at its Rx buffer at the same memory location, it posts a consumed flag at 0x01 of its Tx Buffer. Finally, the producer sees the consumed flag and it updates its 0x01 of the Tx Buffer to 0 from 2. Then, the consumer can ignore the information in 0x02 of its Rx buffer because its header of the information is 0.

5.3.2 Coordinate Rotation

Another important aspect is the rotation of the object's coordinates from FMC. Since the vehicle does not use gimbal system to minimize the total weight and FMC outputs the coordinates of the object in the body frame, the coordinate needs to be rotated back to the earth frame for the robust tracking. The Euler angles are received from the controller MCU, the second Propeller chip in figure 5.1. Then, the fourth Propeller chip reconstructs the rotation matrix. As discussed in chapter 3, the object's relative coordinate in earth frame can be calculated as equation 5.8.

$$\begin{bmatrix} x \\ y \\ z \end{bmatrix}_{ground} = [R] \begin{bmatrix} x \\ y \\ z \end{bmatrix}_{body} \tag{5.8}$$

where [R] is the reconstructed rotation matrix based on the Euler angle. The reconstruction of the rotation matrix can be processed by using equation 3.7.

Chapter 6. Ground Control Software and Communication Protocol

6.1 Overview

To enable monitoring onboard vehicle sated, a miniature ground control station (GCS) was developed. The GCS software is based on Windows operating system and s joystick is connected to it. The software is developed in C# as a WPF application as shown in figure 6.1. The IMU sends out information regarding vehicle states and control outputs to GCS. Also, the GCS can send the control input such as target Euler angles, the motor output for each motor or, interfaced command to take-off or land. Since the information exchanged are digital data, a set of Xbee receiver and transmitter is used. Xbee is a digital interfacing device that works as a serial communication protocol via radio signals.

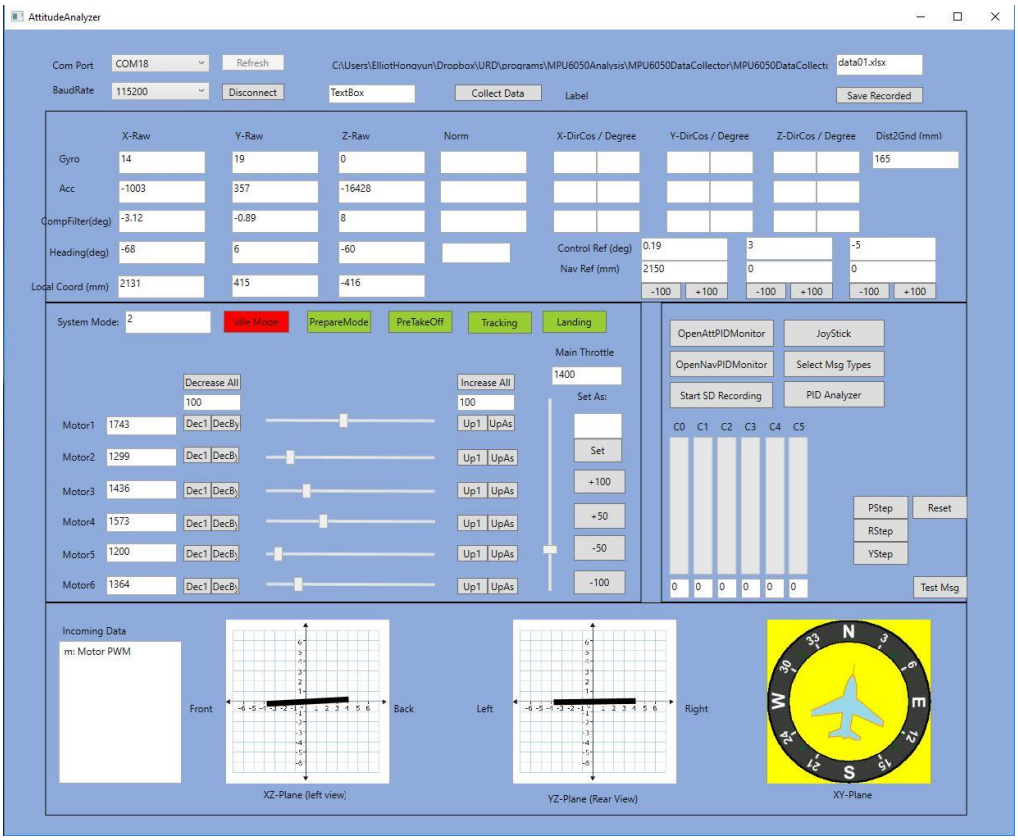

Figure 6.1 Ground Control Software

6.2 Joy Stick Connection

For the use of joystick, SlimDX library is employed in this project [6.1]. The library offers interfaces that simply returns the angle of the stick in x, y, and z rotation and the position of the throttle switch. Then the manual command for the drone is sent via Xbee.

6.3 Communication

Since Xbee module provides an interface that encapsulates low-level radio control so that the user can stay in the serial communication level. In both Spin and C#, the protocol can be considered as character or string type of variables. Each message token is composed of

character and numerical parts. Character part represents the type of information and axis while the numerical part contains the magnitude of the specific value.

6.3.1 Packing Messages from INS

Since Xbee interfaces the communication as serial ports, an array of characters is sent each time. The information is packed as tokens, and the tokens are put as a string. The token is open and closed by the square brackets. For instance, 30 degrees per second of x axis rotation is "[gx30]". The letter g is for angular velocity, x is for axis number, and 30 is the value of the rotation. The letters, '[' and ']', are for packing tokens so that omission of such tokens can be considered as an error or corrupt data, which will be dropped by the parsing algorithm.

6.3.2 Parsing Messages from INS

Since the message from GCS to INS is more likely to be lost or corrupt, minimal character arrays are used to carry the message. For example, instead of using square brackets at the front and last of the token, a semicolon, ';' is used as a separator of each token. As the messages from the GCS arrives, and it is put in a first-in-first-out (FIFO) buffer of the IMU. At each iteration, a byte is read from the FIFO buffer. As before, the first byte of the token is a letter, the second byte is the type or axis number, and the rest bytes are the magnitude. For instance, 'M11200' is to set the motor number 1's PWM as 1200. Unlike C#, Spin language does not have string variable as primitive type. Rather each information is stored in the FIFO buffer as an array of character. To read the one set of the message, a loop should keep reading the FIFO buffer until ';' is reached [55]. To convert the character to 32-bit signed integer, the character variable is subtracted by 48, which is the ASCII code of symbol '0', zero. After converting, the integer is multiplied by 10 and the next integer is added.

Table 6.2 INS parsing algorithm

```
1    int magnitude = 0;
2    char firstLetter = FIFO.readNext();
3    switch (firstLeter)
4        case 'M':
5            char nextByte = FIFO.readNext() - 48;
6            if (nextByte.ASCII < "0" AND nextByte.ASCII > "9" )
7                return;
8            else
9                while (nextByte != ";")
10                   magnitude =  magnitude*10 + (nextByte.ASCII-48)
11               end
12           end
```

6.3.3 Parsing from the Ground Software

Since C# has a string variable as a primitive type, the parsing process is simpler. Also, .Net Framework provides the objects to invoke an event whenever messages from INS arrives. The event function returns a string type variable containing all bytes received after the last evet was invoked. For instance, the literal of the returned string variable can be "[gx-1][gy10][gz8][M11200][M21200]". The literal contains the information of gyroscope x, y, and z axes readings and motor 1, 2, and 3 PWM values. To parse the information, the literal is tokenized and stored in a List<> dynamic memory. With the given example, the List<> would look as shown in figure 6.2.

gx-1	gy10	gz8	M11200	M21200
0x01	0x02	0x03	0x04	0x05

Figure 6.2 Tokens in List<>

Simply, using String.substring() method in C#, the information type, number, and the magnitude can be extracted from the each token in the List<>.

Chapter 7. Conclusion

A hexacopter frame-based UAS was developed. This work contains the developments of INS, FMC, and GCS. Internal algorithms in each part of the project is expected to cooperate without failure. In this section, the summaries of the algorithms and their functionalities are discussed as well as their shortcomings and possible future works.

Hardware components of the vehicle and GCS are shown in chapter 2. The INS is composed of four microcontrollers, two inertial sensors, and a magnetometer. The first microcontroller and the sensors together implement IMU. The second microcontroller implements primarily three algorithms: ESC driver, and attitude and position controllers. The third microcontroller implements message packing parsing algorithms for the GCS. Finally, the fourth microcontroller implements the voltage monitoring and message parsing algorithm for the FMC. For the voltage reading, a voltage divider and follower circuits are developed. With the hardware parts together, the integrated system showed robust and stable performance of the system with the minimal delay. The FMC, yet, does not implement any algorithms managing the battery capacity related to possible flight maneuvers. Optimization techniques regarding the relation between the battery usage and the flight can be developed further.

In chapter 3, the complementary filter algorithm is presented using a rotation matrix. Direct use of the raw sensor values can result in the state estimation with the significant error due to the drift of gyroscope and the inertial force on the accelerometer. To compensate errors from each measurement sources, the complementary filter based on rotation matrix is

implemented to output Euler angles. As shown in chapter 3, the estimated Euler angles show the signals with least noise and negligible delay compared to the raw accelerometer and the integrated gyroscope signals. The update rate for the attitude estimation is approximately 150 Hz. However, the three axes Euler angles can be susceptible to singularities at near 90-degree pitch angles [38]. Therefore, using the quaternions with four axes can be desirable for the robust state estimation.

Color detection and gesture classification algorithms were presented in chapter 4. The color detection algorithm exclusively employees OpenCV library. The color detection algorithm outputs the relative 3D coordinates of an object with a specific color, in this project, a red object is used. The update rate of the relative 3D coordinate is 30Hz. As a future work, using the color detection algorithm, a ground-heading RGB camera and the ultrasonic distance sensor later can be combined for the navigation and landing based on ground markers as well as an adaptation to simultaneous localization and mapping (SLAM) since the color tracking algorithm can lost the reference coordinate location once the object is out of the camera frame. Also, the AI algorithms are implemented to recognize the operator's gesture in real-time. The classification process is comprised of two different steps. Firstly, a Gaussian kernel classifies the skeletal coordinates from the actual human body or the noise. Then, an ANN classifies the human gestures into four possible classes. Since the set of body gestures used in this project has a small number of the distinctive or almost linearly separable features, the classification accuracy shows 100 percent with the single hidden layer ANN. Yet, the cascade of the two AI methods can lower the update rate of the relative coordinate for the position controller. Due to this, the sets gesture input vectors are limited to 4 classes as well as the human-noise classification result is updated once a second. Optimization of the training data set and the classification algorithm is

expected to be processed in the future so that it can interact with more various natural gestures.

In chapter 5, the integration of the onboard computers is shown. Primarily, the attitude and the position controllers are discussed. The PID controllers used for both attitude and position control is a linear controller. The gains of the controllers are adjusted experimentally. The controllers show the stable performance. The stable control performance is achieved for the attitude of the vehicle with small steady state error. Also, position controller performance showed stable oscillation. The steady state oscillation is approximately 0.3 meters. The update rate of the controller is 150Hz for the attitude and 30Hz for the position because the higher frequency is not necessary given the sensor update rate. As a possible future work, the linear controller can be improved to the adaptive nonlinear controller since variables such as the voltage level or payload of the system can affect the controller gains. Indeed, AI algorithms can be fused for the controller gain adjustment or with the controller itself [56]. Next, the internal communication algorithm is presented. Since the Parallax Propeller chip has eight cogs in each module, when more modules are needed, the communication among each other should be enabled. Indeed, the four MCU boards used show the robust communication ability by performing the flight in real-time with GCS, onboard computer, and the human operator for the drone.

Lastly, in chapter 6, the development of the GCS is showed. Based on the C# SerialPort object, communication with the microcontrollers could be simply achieved. The main focus of the GCS is message packing and parsing rules. The messages can be divided into tokens as the string variable; then the tokens can be further divided into the type, axis, and magnitude. With the GCS, the functionalities of the collecting data, sending inputs, and monitoring the onboard states are successfully implemented. Since many types of onboard states are communicated via

a digital radio module, Xbee, the longer messages tend to end up with the higher error rate. To augment the communication accuracy, multiple Xbee modules with multiple channels can be used in the future. Also, the binary information that carries byte arrays can be directly interpreted as both character and signed integers rather than all-character in the array to minimize the amount of the bit-wise information.

References

1. Misener, P., Amazon Petition for Exemption, 2014.

2. Tvaryanas, A.P., Thompson, B.T. & Constable, S.H., U.S. Military Unmanned Aerial Vehicle Mishaps: Assessment of the Role of Human Factors using HFACS, Technical Report, Brooks City-Base, TX, USAF Human Performance Directorate, 2005.

3. Drury, J., & Scott, S., Awareness in Unmanned Aerial Vehicle Operations, The International C2, 2008

4. Call, B., & Barber, B. Obstacle Avoidance For Unmanned Air Vehicles Using Image Feature Tracking, AIAA, 2006-6541, 2006.

5. Whitfield, C., An Adaptive Dual-Optimal Path-Planning Technique for Unmanned Air Vehicles with Application to Solar-Regenerative High Altitude Long Endurance Flight, The Ohio State University, 2009.

6. R.A. Bolt, Put-that-there: voice and gesture at the graphics interface, in: Proc. Siggraph, ACM, NY, 1980, pp. 262–270.

7. Apple, Siri website, 2017, https://support.apple.com/en-us/HT204389.

8. Google, voice search website, https://www.google.com/search/about/features/01.

9. Microsoft, Kinect website, 2017, https://msdn.microsoft.com/en-us/library/hh438998.aspx.

10. Sony, Playstation camera website, 2016, https://www.playstation.com/en-us/explore/accessories/playstation-camera-ps4/.

11. Guanglong Du, Ping Zhang, Jianhua Mai and Zeling Li, Markerless kinect-based hand tracking for robot teleoperation, International Journal of Advanced Robotic Systems 9, 2012.

12. Eiji Machida, Meifen Cao, Toshiyuki Murao, Hiroshi Hashimot, Human motion tracking of mobile robot with Kinect 3D sensor, Proceedings of SICE Annual Conference (SICE), 2012.

13. Foti Coleca ; Sascha Klement ; Thomas Martinetz and Erhardt Barth, Real-time skeleton tracking for embedded systems, Proc. SPIE 8667, Multimedia Content and Mobile Devices, 86671X (March 7, 2013); doi:10.1117/12.2003004; http://dx.doi.org/10.1117/12.2003004.

14. Armin Ambühl, Interaction with a Quadrotor via the Kinect, ETH Zurich, 2011, http://www.youtube.com/watch?v=A52FqfOi0Ek.

15. Sanna, Andrea, Fabrizio Lamberti, Gianluca Paravati, and Federico Manuri. A Kinect-based natural interface for quadrotor control. international Federation for Information Processing, 2013. pp. 179-86. Elsevier.

16. Chi-Tinh Dang, H. Pham, Thanh-Binh Pham and Nguyen-Vu Truong, "Vision based ground object tracking using AR.Drone quadrotor," 2013 International Conference on Control, Automation and Information Sciences (ICCAIS), Nha Trang, 2013, pp. 146-151.

17. N. Thiang, LuMaw, H. M. Tun, Vision-Based Object Tracking Algorithm With AR. Drone, International Journal of Scientific & Technology Research Vol. 5, issue 06, June 2016.

18. Helipal, Tarot FY 680, 2017, http://www.helipal.com/tarot-fy680-pro-hexacopter-frame-set.html.

19. Parrot, A.R drone, 2016, https://www.parrot.com/us/drones/parrot-ardrone-20-gps-edition#parrot-ar-drone-20-gps-edition .

20. University of Southern California, FAAST web site, http://projects.ict.usc.edu/mxr/faast/.

21. Helipal, DJI E800 Propulsion system, 2017, http://www.helipal.com/dji-e800-6-props-super-propulsion-system.html

22. Intel, Intel NUC, 2017, http://www.intel.com/content/www/us/en/nuc/nuc-kit-nuc5i7ryh.html.

23. Parallax, Propeller ASC, 2017, https://www.parallax.com/product/32214.

24. InvenSense, MPU-9250, 2017, https://www.invensense.com/products/motion-tracking/9-axis/mpu-9250/.

25. Parallax, Ping Ultrasonic Distance Sensor, https://www.parallax.com/product/28015.

26. SlimDX, website, 2011, https://slimdx.org/.

27. Digi, Xbee Pro, 2017, https://www.digi.com/products/xbee-rf-solutions/embedded-rf-modules-modems/xbee-pro-900hp.

28. Leishman, J. Gordon. Helicopter aerodynamics. 2nd ed. Cambridge: Cambridge U Press, 2000. Print.

29. Parallax, HMC5883L, https://www.parallax.com/product/29133.

30. NXP Semiconductors, UM10204, 2014, http://www.nxp.com/documents/user_manual/UM10204.pdf.

31. Eagle, website, https://cadsoft.io/#.

32. Mini-box, DCDC-USB-200, 2016, http://www.mini-box.com/DCDC-USB-200.

33. Dorf, Richard C., and James A. Svoboda. Introduction to electric circuits. 7th ed. Hoboken, NJ: J. Wiley & Sons, 2006. Print.

34. EmguCV, website, 2017, http://www.emgu.com/wiki/index.php/Main_Page.

35. OpenCV, website, 2017, http://opencv.org/.

36. Schmidt, D. K. Modern flight dynamics. New York, NY: McGraw-Hill, 2012.

37. Premerlani, W. and Bizard, P., Direction cosine matrix IMU: Theory (DCMDraft2), May 17 2009.

38. McCrink, M., Development of Flight-Test Performance Estimation Techniques for Small Unmanned Aerial Systems, The Ohio State University, 2015

39. Fernando, Shermal Ruwantha. "Color Detection & Object Tracking." Color Detection & Object Tracking. Sept. 2010. Web. 25 Dec. 2016.

40. Burge, M., Burger, W. Digital Image Processing: An Algorithmic Introduction using Java. New York, NY: Springer, 2008.

41. Haykin, Simon S. Neural Networks and Learning Machines. 3rd ed. New York: Prentice Hall/Pearson, 2009. Print.

42. Fisher, R., S. Perkins, A. Walker, and E. Wolfart. "Structuring Elements." Glossary - Structuring Elements. N.p., 2003. http://homepages.inf.ed.ac.uk/rbf/HIPR2/strctel.htm.

43. Suzuki, S. and Abe, K., Topological Structural Analysis of Digitized Binary Images by Border Following. CVGIP 30 1, pp 32-46 (1985)

44. Smeenk, Roland. "Kinect V1 and Kinect V2 fields of view compared." Roland Smeenk. N.p., 11 Mar. 2014. http://smeenk.com/kinect-field-of-view-comparison/.

45. Wang, D. “Multi-Layer Perceptron”, CSE 5526. The Ohio State Universtiy, Columbus, Fall Semester 2016. Lecture.

46. Lee, H., Hello *키넥트 - 예제 중심 프로그래밍-* [Hello Kinect - example based programming -]. Seoul, Korea: *홍릉과학출판사*. 2013.

47. Jamie Shotton, Andrew Fitzgibbon, Andrew Blake, Alex Kipman, Mark Finocchio, Richard Moore, Toby Sharp, "Real-Time Human Pose Recognition in Parts from a Single Depth Image", IEEE, June 2011.

48. Belkin, M., CSE 5523. "Machine Learning and Statistical Pattern Recognition", The Ohio State University, Columbus, Spring Semester 2016. Lecture.

49. Gretton, A, Introduction to RKHS, and some simple kernel algorithms, Gatsby Computational Neuroscience Unit, London's Global University, 2016. http://www.gatsby.ucl.ac.uk/~gretton/coursefiles/lecture4_introToRKHS.pdf

50. Devore, Jay L. Probability and statistics for engineering and the sciences. 8th ed. S.l.: Brooks/Cole Cengage Learning, 2011. Print.

51. Fernando Bevilacqua, Finite-State Machines: Theory and Implementation, Oct. 2013, https://gamedevelopment.tutsplus.com/tutorials/finite-state-machines-theory-and-implementation--gamedev-11867.

52. Ogata, Katsuhiko. Modern control engineering. 5th ed. Upper Saddle River, NJ: Prentice Hall, 2010. Print.

53. Silberschatz, Abraham, Peter B. Galvin, and Greg Gagne. Operating system concepts. 9th ed. Hoboken, NJ: J. Wiley & Sons, 2005. Print.

54. Yedavalli, R. (2015). AAE 3521 Flight Vehicle Dynamics. Unpublished class note.

55. JonnyMac, "Two Propeller Communication" Online discussion., May 2016, Parallax Forum, http://forums.parallax.com/discussion/164181/two-propeller-communication/p1

56. Felix Berkenkamp, Angela P. Schoellig, Andreas Krause, "Safe controller optimization for quadrotors with Gaussian processes", in Proc. of the IEEE International Conference on Robotics and Automation (ICRA), 2016, pp. 493-496

Appendix A. Cross Validation

This section shows cross validation technique used in Gaussian kernel method in chapter 4. Figure A.1 shows the training data set. The first column indicates the class label while second to twenty second columns indicate the data to input. The kernel methods finds the linear combination of the input data that can result in 1 or 2. However, there are two unknown terms σ and λ, the mean of the standard deviation of the Gaussian and the regularization constant respectively. These two unknown terms can be set by cross validation. In this work, 5-fold cross validation is attempted.

1	X1	X2	X3	X4	X5	X6	X7	…	x21
1	X1	X2	X3	X4	X5	X6	X7	…	x21
1	X1	X2	X3	X4	X5	X6	X7	…	x21
1	X1	X2	X3	X4	X5	X6	X7	…	x21
…	X1	X2	X3	X4	X5	X6	X7	…	x21
2	X1	X2	X3	X4	X5	X6	X7	…	x21
2	X1	X2	X3	X4	X5	X6	X7	…	x21
2	X1	X2	X3	X4	X5	X6	X7	…	x21
2	X1	X2	X3	X4	X5	X6	X7	…	x21

Figure A.1 Training Set

Once the training set is ready, the data is divided by 5 sections. Since there are 5 different validation sets, the score from the each set can be calculated and added for a combination of σ and λ. When the predicted and actual labels match, the 1 is added to the score.

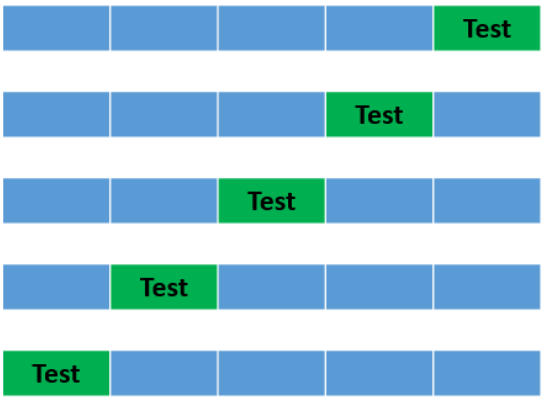

Figure A.2 5-fold cross validation

Also, various test values for σ and λ is selected. For instance, $\sigma = 0.1, 0.2, 0.3, 0.4, and\ 0.5, \lambda = 10^{-1}, 10^{-2}, 10^{-3}, 10^{-4}, and 10^{-5}$ are used and total $5 \times 5 \times 5 = 125$ iterations are processed.

Table A.1 shows the result of the 5-fold cross validation. The numbers are the score due to the combination of each σ and λ. In this specific example, $\sigma = 0.2$ and $\lambda = 10^{-15}$are used since the score is the highest. Based on these numbers, the regular training algorithm discussed in chapter 4 can be processed.

Table A.1 5-fold cross validation result

	$\lambda = 10^{-5}$	$\lambda = 10^{-10}$	$\lambda = 10^{-15}$	$\lambda = 10^{-20}$	$\lambda = 10^{-30}$
$\sigma = 0.05$	812	862	862	862	862
$\sigma = 0.1$	980	1270	1270	1270	1270
$\sigma = 0.2$	1034	1568	1572	1572	1572
$\sigma = 0.3$	1066	1502	1470	1470	1470
$\sigma = 0.4$	1074	1392	1410	1410	1410